Quarterly Technical Report

Solid State Research

19960621 094

1995:4

Lincoln Laboratory

MASSACHUSETTS INSTITUTE OF TECHNOLOGY

LEXINGTON, MASSACHUSETTS

This technical report has been reviewed and is approved for publication.

FOR THE COMMANDER
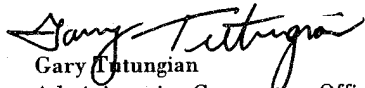
Gary Tutungian
Administrative Contracting Officer
Contracted Support Management

MASSACHUSETTS INSTITUTE OF TECHNOLOGY
LINCOLN LABORATORY

SOLID STATE RESEARCH

QUARTERLY TECHNICAL REPORT

1 AUGUST–31 OCTOBER 1995

ISSUED 17 JUNE 1996

LEXINGTON   MASSACHUSETTS

ABSTRACT

This report covers in detail the research work of the Solid State Division at Lincoln Laboratory for the period 1 August through 31 October 1995. The topics covered are Electrooptical Devices, Quantum Electronics, Materials Research, Submicrometer Technology, High Speed Electronics, Microelectronics, Analog Device Technology, and Digital Integrated Circuits. Funding is provided primarily by the Air Force, with additional support provided by the Army, ARPA, Navy, BMDO, NASA, and NIST.

TABLE OF CONTENTS

LIST OF ILLUSTRATIONS

LIST OF ILLUSTRATIONS (Continued)

LIST OF ILLUSTRATIONS (Continued)

LIST OF TABLES

INTRODUCTION

1. ELECTROOPTICAL DEVICES

A simple scheme has been developed for calculation of the Strehl ratio and mode coupling efficiency. Accurate large-numerical-aperture microlenses and precision optical alignment are needed for efficient coupling of diode lasers to single-mode fibers or waveguides, and this scheme is useful for quick diagnosis of the optical system and helpful in guiding the microlens design and fabrication.

2. QUANTUM ELECTRONICS

First, second, third, fourth, and fifth harmonics of the output of a fiber-pumped passively Q-switched Nd:YAG microchip laser have been obtained at pulse energies of 8.0, 3.5, 0.3, 0.7, and 0.01 μJ, respectively, in an optical head occupying a volume < 3 cm^3. This compact, economic, all-solid-state source provides coherent, subnanosecond, multikilowatt pulses in the infrared, visible, and/or ultraviolet at repetition rates in excess of 10 kHz.

3. MATERIALS RESEARCH

High-quality $Pb_{1-x}Eu_xTe/PbTe$ multiple quantum wells (MQWs) have been grown by molecular beam epitaxy, and their measured Seebeck coefficients at 300 K were found to be about twice that of the best bulk PbTe. This is the first detailed experimental investigation of MQW structures designed to improve the thermoelectic figure of merit ZT, and the value of $Z_{2D}T$ > 1.2 achieved for these PbTe quantum wells has broken the decades-long $ZT \cong 1$ barrier for a room-temperature thermoelectric material.

4. SUBMICROMETER TECHNOLOGY

Plasma-deposited carbon-based polymer films have been developed for use as a dry-deposited, dry-developed positive-tone photoresist for 193-nm lithography. These films crosslink upon exposure to 193-nm radiation, enabling selective silicon uptake via reaction of silylamine gas with hydroxyl in the film.

Field emission of electrons has been demonstrated from nitrogen-doped diamond at fields < 0.1 V μm^{-1}. Although the vacuum field is small, these electrons have energies of several kilovolts and are emitted from the surface in well-defined beamlets.

5. HIGH SPEED ELECTRONICS

GaAs complementary metal-insulator-semiconductor field-effect transistors (MISFETs) with a low-temperature-grown GaAs gate insulator have been fabricated using the same epitaxial layer structure with self-aligned Si and Be implants. The maximum drain current is 40 and 120 mA/mm for a normally-off n- and p-channel MISFET, respectively, and increases to 500 mA/mm for a normally-on n-channel device.

6. MICROELECTRONICS

The signal variance of photoelectrons collected in the well of an electronically shuttered, back-illuminated charge-coupled device has been measured to be substantially less than the expected shot noise of the incident light. Under certain conditions there is a factor of 1.75 improvement in the squared signal-to-noise ratio.

7. ANALOG DEVICE TECHNOLOGY

Third-order intermodulation power generated by a Josephson junction in a $YBa_2Cu_3O_{7-x}$ microwave resonator has been measured and compared to a calculation based on the resistively shunted junction model. The results, which are relevant to the coupled-grain model used to describe microwave properties of high-T_c superconductors and to the understanding of Josephson junctions in these materials, agree with junction parameters determined by power-dependent loss measurements on the same resonator.

8. DIGITAL INTEGRATED CIRCUITS

A decoded version of the ultradense, once-programmable, read-only memory has been designed and is in fabrication. The program goal is to build a memory with bit dimensions approaching the lithographic pitch, and components such as single bits at 0.25-μm diameter and undecoded arrays have been demonstrated.

REPORTS ON SOLID STATE RESEARCH

1 AUGUST THROUGH 31 OCTOBER 1995

PUBLICATIONS

Electrical Properties of the Hydrogen Defect in InP and the Microscopic Structure of the 2316 cm^{-1} Hydrogen Related Line	D. F. Bliss* G. G. Bryant* D. Gabbe* G. W. Iseler E. E. Haller* F. X. Zach*	*Proceedings of the 7th International Conference on Indium Phosphide and Related Materials* (IEEE, New York, 1995), p. 678
Large Electromagnetic Stop Bands in Metallodielectric Photonic Crystals	E. R. Brown O. B. McMahon	*Appl. Phys. Lett.* **67**, 2138 (1995)
InAsSb/InAlAsSb Strained Quantum-Well Diode Lasers Emitting at 3.9 μm	H. K. Choi G. W. Turner	*Appl. Phys. Lett.* **67**, 332 (1995)
Tunable Single-Frequency Yb:YAG Laser with 1-W Output Power Using Twisted-Mode Technique	T. Y. Fan J. Ochoa	*IEEE Photon. Technol. Lett.* **7**, 1137 (1995)
All-Dry Resist Processes for 193-nm Lithography	M. W. Horn B. E. Maxwell R. R. Kunz M. S. Hibbs* L. M. Eriksen S. C. Palmateer A. R. Forte	*Proc. SPIE* **2438**, 760 (1995)
Spectral Linewidth of a Free-Running Continuous-Wave Single-Frequency External-Cavity Quantum-Well InGaAs/AlGaAs Diode Laser	L. Hsu* A. Mooradian* R. L. Aggarwal	*Opt. Lett.* **20**, 1788 (1995)

---

*Author not at Lincoln Laboratory.

Near-Diffraction-Limited High Power (~ 1 W) CW Single Longitudinal Mode Diode Laser Tunable from 960 to 980 nm	R. J. Jones* S. Gupta* R. K. Jain* J. N. Walpole	*Electron. Lett.* **31**, 1668 (1995)
CH$_3$I Vapor Etching of Masked and Patterned GaAs	C. W. Krueger C. A. Wang D. Hsieh* M. Flytzani- Stephanopoulos*	*J. Cryst. Growth* **153**, 81 (1995)
Observation of a Nanocrystalline-to-Amorphous Phase Transition in Luminescent Porous Silicon	R. R. Kunz P. M. Nitishin H. R. Clark M. Rothschild B. Ahern*	*Appl. Phys. Lett.* **67**, 1766 (1995)
High-Power Diode-Pumped Mid-Infrared Semiconductor Lasers	H. Q. Le G. W. Turner H. K. Choi J. Ochoa A. Sanchez J. M. Arias* M. Zandian* R. Zucca* Y.-Z. Liu*	*Proc. SPIE* **2382**, 262 (1995)
Theoretical Analysis of Gain in Compressive Strained Quantum Well InAlAsSb/GaSb Structures for 3–4 μm Lasers	R. F. Nabiev* C. J. Chang- Hasnain* H. K. Choi	*OSA Tech. Dig. Ser.* **20**, 31 (1995)
Ho:YAG Laser Pumped by 1.9-μm Diode Lasers	C. D. Nabors* J. Ochoa T. Y. Fan A. Sanchez H. K. Choi G. W. Turner	*IEEE J. Quantum Electron.* **31**, 1603 (1995)

---

*Author not at Lincoln Laboratory.

Optimization of a 193-nm Silylation Process for Sub-0.25-μm Lithography	S. C. Palmateer R. R. Kunz M. W. Horn A. R. Forte M. Rothschild	*Proc. SPIE* **2438**, 455 (1995)
193-nm Lithography	M. Rothschild A. R. Forte M. W. Horn R. R. Kunz S. C. Palmateer J. H. C. Sedlacek	*IEEE J. Select. Topics Quantum Electron.* **1**, 916 (1995)
High-Power YBCO Microwave Filters and Their Nonlinearities	T. C. L. G. Sollner A. C. Anderson W. G. Lyons D. E. Oates R. W. Ralston J. P. Sage P. Polakos* P. Mankiewich* E. De Obaldia* X. Ma* R. Miller*	*Proceedings of the Fifth International Superconductive Electronics Conference* (ISEC, Nagoya, Japan, 1995), p. 12-2
Analysis of N × M Waveguide Splitters and Couplers with Multimode Guiding Sections	E. R. Thoen* L. A. Molter* J. P. Donnelly	In *Guided-Wave Optoelectronics: Device Characterization, Analysis, and Design*, T. Tamir, G. Griffel, and H. L. Bertoni, eds. (Plenum, New York, 1995)
Tritertiarybutylaluminum as an Organometallic Source for Epitaxial Growth of AlGaSb	C. A. Wang M. C. Finn S. Salim* K. F. Jensen* A. C. Jones*	*Appl. Phys. Lett.* **67**, 1384 (1995)

*Author not at Lincoln Laboratory.

ACCEPTED FOR PUBLICATION

Frequency and Temperature Dependence of Z_s of $YBa_2Cu_3O_{7-\delta}$ Thin Films in a DC Magnetic Field: Investigation of Vortex Dynamics	N. Belk* D. E. Oates D. A. Feld G. Dresselhaus* M. S. Dresselhaus*	*Phys. Rev. B*
Comparison of Electric Field Emission from Nitrogen-Doped, Type Ib and Boron-Doped Diamond	M. W. Geis	*Appl. Phys. Lett.*
High Thermoelectric Figures of Merit in PbTe Quantum Wells	T. C. Harman D. L. Spears M. J. Manfra	*J. Electron. Mater.*
Plasma-Deposited Silylation Resist for 193-nm Lithography	M. W. Horn M. Rothschild B. E. Maxwell R. B. Goodman R. R. Kunz L. M. Eriksen	*Appl. Phys. Lett.*
CH_3I Vapor Etching of GaAs in a Vertical Rotating-Disk Reactor	C. W. Krueger S. Patnaik* C. A. Wang M. Flytzani-Stephanopoulos*	*J. Cryst. Growth*
Auger Lifetime in InAs, InAsSb, and InAsSb-InAlAsSb Quantum Wells	J. R. Lindle* J. R. Meyer* C. A. Hoffman* F. J. Bartoli* G. W. Turner H. K. Choi	*Appl. Phys. Lett.*
Terahertz Photomixing in Low-Temperature-Grown GaAs	K. A. McIntosh E. R. Brown K. B. Nichols O. B. McMahon	*Appl. Phys. Lett.*

*Author not at Lincoln Laboratory.

Nonlinear Surface Impedance of YBCO Thin Films: Measurements, Modeling and Effects in Devices	D. E. Oates P. P. Nguyen* G. Dresselhaus* M. S. Dresselhaus* G. Koren* E. Polturak*	*J. Superconduct.*
Microwave Power Dependence of $YBa_2Cu_3O_7$ Thin-Film Josephson Edge Junctions	D. E. Oates P. P. Nguyen* Y. Habib* G. Dresselhaus* M. S. Dresselhaus* G. Koren* E. Polturak*	*Appl. Phys. Lett.*
Binary Optics: A VLSI-Based Microoptics Technology	M. B. Stern	*Microelectron. Eng.*
Room-Temperature 50-mJ/Pulse Side-Diode-Pumped Yb:YAG Laser	D. S. Sumida* T. Y. Fan	*Opt. Lett.*
n-AlGaSb and GaSb/AlGaSb Double-Heterostructure Lasers Grown by Organometallic Vapor Phase Epitaxy	C. A. Wang K. F. Jensen* A. C. Jónes* H. K. Choi	*Appl. Phys. Lett.*

*Author not at Lincoln Laboratory.

PRESENTATIONS[†]

Single-Layer Photoresists for 193-nm Lithography	R. D. Allen* G. M. Wallraff* I. Y. Wan* R. A. DiPietro* D. C. Hofer* W. E. Conley* R. R. Kunz	
Plasma-Deposited Silylation Resist for 193-nm Lithography	M. W. Horn B. E. Maxwell R. B. Goodman R. R. Kunz L. M. Eriksen	
Limits to Etch Resistance for 193-nm Single-Layer Resists	R. R. Kunz S. C. Palmateer A. R. Forte R. D. Allen* G. M. Wallraff* R. A. DiPietro* D. C. Hofer*	1st International Symposium on 193-nm Lithography, Colorado Springs, Colorado, 15-18 August 1995
Optimization of a 193-nm Silylation Process for Sub-0.25-μm Lithography	S. C. Palmateer A. R. Forte R. R. Kunz M. W. Horn M. Rothschild	
Optical Materials for 193-nm Lithography	M. Rothschild J. H. C. Sedlacek R. Schenker* W. G. Oldham* A. Grenville	

---

*Author not at Lincoln Laboratory.

[†]Titles of presentations are listed for information only. No copies are available for distribution.

Diamond Emitters: Fabrication and Theory	M. W. Geis	Applied Diamond
	J. C. Twichell	Conference '95,
	M. B. Stern	Gaithersburg, Maryland,
	N. N. Efremow	21-24 August 1995
	K. E. Krohn	
	T. M. Lyszczarz	
	R. Uttaro	

Diamond Emitters: Fabrication and
Theory

M. W. Geis
J. C. Twichell
M. B. Stern
N. N. Efremow
K. E. Krohn
T. M. Lyszczarz
R. Uttaro

Applied Diamond
Conference '95,
Gaithersburg, Maryland,
21-24 August 1995

Coulomb Blockade in a Silicon MOS
Single Electron Transistor

D. Abusch-Magder
T. M. Lyszczarz
D. C. Shaver
C. Dennis

NATO Advanced Study
Institute: Quantum Transport
in Semiconductor Submicron
Structures,
Bad Lauterberg, Germany,
21-31 August 1995

Diamond Cold Cathodes: Experiment
and Theory

J. C. Twichell
M. W. Geis
T. M. Lyszczarz
K. E. Krohn
N. N. Efremow
C. A. Marchi

Diamond Films '95,
Barcelona, Spain,
10-15 September 1995

Dielectric/Metal Hybrid Photonic
Crystals and Their Applications

E. R. Brown
O. B. McMahon
L. J. Mahoney
K. M. Molvar

Optical Society of America
Annual Meeting,
Portland, Oregon,
10-15 September 1995

Profile Control in Resist Dry
Development for Sub-0.25-μm
Lithography

M. W. Horn
S. C. Palmateer
R. R. Kunz
A. R. Forte

Plasma Etch Users Group
Symposium,
Sunnyvale, California,
11 September 1995

Results of Oil Thickness Measurements
at OHMSETT Using a Frequency
Scanning Microwave Radiometer

T. J. Murphy
O. B. McMahon
E. R. Brown
G. L. Hover*

3rd Thematic Conference on
Remote Sensing for Marine
and Coastal Environment,
Seattle, Washington,
18-20 September 1995

---

*Author not at Lincoln Laboratory.

Solid-State Laser Development at Lincoln Laboratory	T. Y. Fan	Technical Seminar, University of Rhode Island, Kingston, Rhode Island, 19 September 1995; Meeting of the Boston Chapter, IEEE Lasers and Electro-Optics Society, Lexington, Massachusetts, 21 September 1995
Laser-Based Active Optical Remote Sensing	T. Y. Fan	Technical Seminar, University of Massachusetts, Amherst, Massachusetts, 25 September 1995
Optical Interconnections for Digital Systems	D. Z. Tsang	Lincoln Laboratory Technical Seminar Series, University of Illinois, Urbana, Illinois, 4 October 1995
Progress in the Development of a Superconductive Crossbar Switch	D. A. Feld	Workshop on Superconductive Electronics: Devices, Circuits, and Systems, Farmington, Pennsylvania, 8-12 October 1995
Superconductive Circuits for a 2-GHz Spread-Spectrum Modem	J. P. Sage	
A New Terahertz Photomixer for Far-Infrared Spectroscopy of Atmospheric Species	A. S. Pine* R. D. Suenram* E. R. Brown K. A. McIntosh	Meeting of the American Astronomical Society, Manua Laui, Hawaii, 13 October 1995
Diamond Cold Cathodes: Experiment and Theory	M. W. Geis T. C. Twichell T. M. Lyszczarz K. E. Krohn N. N. Efremow C. A. Marchi	General Electric Super Abrasives Meeting, Schenectady, New York, 15 October 1995

*Author not at Lincoln Laboratory.

Dry Development of Sub-0.25-μm Features Patterned with 193-nm Silylation Resist	S. C. Palmateer A. R. Forte R. R. Kunz M. W. Horn	42nd National Symposium of the American Vacuum Society, Minneapolis, Minnesota, 16-20 October 1995
High-Frequency Quantum-Well Infrared Photodetectors	H. C. Liu* J. Li* E. R. Brown K. A. McIntosh	International Conference on Intersubband Transitions in Quantum Wells, Kibbutz Ginosar, Israel, 23-26 October 1995
Tunable Single-Frequency Yb:YAG Laser with 1-W Output Power	T. Y. Fan J. Ochoa	IEEE Lasers and Electro-Optics Society Annual Meeting, San Francisco, California, 30 October–2 November 1995

---

*Author not at Lincoln Laboratory.

ORGANIZATION

SOLID STATE DIVISION

D. C. Shaver, *Head*
I. Melngailis, *Associate Head*
J. F. Goodwin, *Assistant*

A. L. McWhorter, *Fellow*
C. L. Keast, *Staff*
D. Abusch-Magder, *Research Assistant*
T. M. Bloomstein, *Research Assistant*
J. T. Chiou, *Research Assistant*
J. P. Mattia, *Research Assistant*
N. L. DeMeo, Jr., *Associate Staff*
J. W. Caunt, *Assistant Staff*
K. J. Challberg, *Administrative Staff*

SUBMICROMETER TECHNOLOGY

M. Rothschild, *Leader*
T. M. Lyszczarz, *Assistant Leader*
L. H. Dubois, *Senior Staff*†

Astolfi, D. K.	Kunz, R. R.
Craig, D. M.	Liu, H.
DiNatale, W. F.	Maki, P. A.
Doran, S. P.	Palmateer, S. C.
Efremow, N. N., Jr.	Reinold, J. H., Jr.
Forte, A. R.	Sedlacek, J. H. C.
Geis, M. W.	Stern, M. B.
Goodman, R. B.	Twichell, J. C.
Hartney, M. A.	Uttaro, R. S.
Horn, M. W.	

QUANTUM ELECTRONICS

A. Sanchez-Rubio, *Leader*
T. Y. Fan, *Assistant Leader*

Aggarwal, R. L.	Jeys, T. H.
Cook, C. C.	Kelley, P. L.‡
Daneu, V.	Le, H. Q.
DeFeo, W. E.	Ochoa, J. R.
DiCecca, S.	Zayhowski, J. J.
Dill, C., III	

ELECTRONIC MATERIALS

B-Y. Tsaur, *Leader*
D. L. Spears, *Assistant Leader*

Chen, C. K.	Manfra, M. J.
Choi, H. K.	McGilvary, W. L.
Connors, M. K.	Nitishin, P. M.
Foley, L. J.*	Paul, S. A.*
Harman, T. C.	Santigo, D. D.
Herrmann, F. P.	Turner, G. W.
Iseler, G. W.	Wang, C. A.
Krohn, L., Jr.	

HIGH SPEED ELECTRONICS

M. A. Hollis, *Leader*
E. R. Brown, *Assistant Leader*
R. A. Murphy, *Senior Staff*

Bozler, C. O.	McMahon, O. B.
Chen, C. L.	Molnar, R. J.
Harris, C. T.	Nichols, K. B.
Lincoln, G. A., Jr	Rabe, S.
Mahoney, L. J.	Rathman, D. D
Mathews, R. H.	Verghese, S.
McIntosh, K. A.	

---

* Research Assistant
†Intergovernmental Personnel Act assignment
‡Leave of Absence

ELECTROOPTICAL DEVICES

R. C. Williamson, *Leader*
L. M. Johnson, *Assistant Leader*

Aull, B. F.	Missaggia, L. J.
Bailey, R. J.	Mull, D. E.
Betts, G. E.	O'Donnell, F. J.
Donnelly, J. P.	Palmacci, S. T.
Goodhue, W. D.	Poillucci, R. J.
Groves, S. H.	Reeder, R. E.
Hovey, D. L.	Tsang, D. Z.
Liau, Z. L.	Walpole, J. N.

ANALOG DEVICE TECHNOLOGY

R. W. Ralston, *Leader*
T. C. L. G. Sollner, *Assistant Leader*
A. C. Anderson, *Senior Staff*

Arsenault, D. R.	Lyons, W. G.
Boisvert, R. R.	Macedo, E. M., Jr.
Brogan, W. T.	McClure, D. W.
Feld, D. A.	Murphy, P. G.
Fitch, G. L.	Oates, D. E.
Gleason, E. F.	Sage, J. P.
Ham, J. M.	Seaver, M. M.
Holtham, J. H.	Slattery, R. L.

MICROELECTRONICS

E. D. Savoye, *Leader*
B. B. Kosicki, *Assistant Leader*
B. E. Burke, *Senior Staff*

Clark, H. R., Jr.	Johnson, K. F.
Daniels, P. J.	Lind, T. A.
Doherty, C. L., Jr.	Loomis, A. H.
Dolat, V. S.	McGonagle, W. H.
Donahue, K. G.	Mountain, R. W.
Donahue, T. C.	Percival, K. A.
Felton, B. J.	Reich, R. K.
Gregory, J. A.	Young, D. J.
Hotaling, T. C.	

DIGITAL INTEGRATED CIRCUITS

J. I. Raffel, *Leader*
P. W. Wyatt, *Associate Leader*
A. H. Anderson, *Senior Staff*

Berger, R.	Howard, J. F.
Burns, J. A.	Knecht, J. M.
Davis, P. V.	Newcomb, K. L.
D'Onofrio, R. P.	Soares, A. M.
Frankel, R. S.	Wachtmann, B. K.
Fritze, M.	Young, G. R.
Herndon, T. O.	

1. ELECTROOPTICAL DEVICES

1.1 SIMPLE SCHEME FOR ANALYSIS OF DIODE LASER MICROOPTICS

The interest in microoptics for use with diode lasers has been increasing. Microoptics can be used for collimating the laser output or for efficient coupling of optical powers into single-mode fibers or waveguides [1]. Because of the relatively large divergence of the output from a diode laser, large-numerical-aperture microlenses are needed and high degrees of accuracy are also required for the optical alignment [1]. In this work, we use a simple analytical technique that is capable of quick diagnosis of the optical system and is highly desirable for the microlens design and fabrication.

Figure 1-1 shows a collimating microlens in front of a point source. By equating the optical path lengths SP and SOQ, one can readily derive the lens profile:

$$z = \frac{f_0}{n+1}\left[-1 + \sqrt{1 + \frac{n+1}{n-1}\left(\frac{y}{f_0}\right)^2}\right],$$

(1.1)

where n is the refractive index of the lens material. This is the well-known hyperbolic profile for exact collimation of a point source without any aberration. At large numerical apertures, however, small deviations from this ideal lens profile or inaccuracies in the alignment to the source can result in severe aberrations. In this work, we first consider a special type of deviation that is important for mass-transported microlenses [2]–[4], but the analysis technique is rather generally applicable to other types of errors.

271193-1
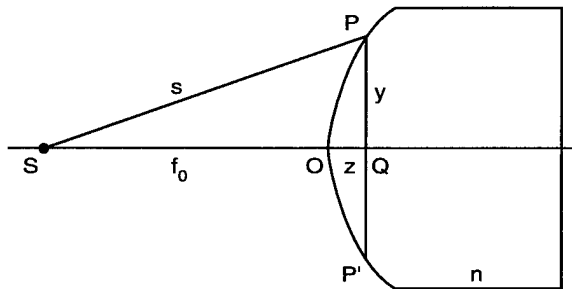
Figure 1-1. Microlens for collimation of a point source. By considering the optical path lengths, phase distortion in the plane PP′ can readily be calculated for any deviation from the ideal lens profile and the precise optical alignment. The phase deviations can in turn be used to predict the lens performance.

1

One frequent error in the mass-transported microlenses is the size of the lens sag, which arises from inaccurate etched mesa height in the fabrication of the lens preform [2],[3]. When the preform is overetched by a small fraction ε, the lens profile becomes

$$z' = (1+\varepsilon)\frac{f_0}{n+1}\left[-1+\sqrt{1+\frac{n+1}{n-1}\left(\frac{y}{f_0}\right)^2}\right] , \tag{1.2}$$

where f_0 is the designed focal length. For small numerical apertures, this simply results in a change of effective focal length from f_0 to

$$f' = f_0/(1+\varepsilon) , \tag{1.3}$$

without significant degradation in lens performance. However, if the source is placed at the correct focal length f', the output is only approximately collimated. For larger numerical apertures, there is an increasing phase-front distortion, which can be calculated by evaluating the optical path length difference

$$\delta = s - f' - nz' , \tag{1.4}$$

with

$$s = \sqrt{(f'+z')^2 + y^2} . \tag{1.5}$$

The calculated phase variation across the lens aperture can in turn be used to predict the lens performance. The solid trace in Figure 1-2 shows the calculated phase variation for $f_0 = 160 \ \mu$m and $\varepsilon = 0.1$. Note that the phase deviation has a predominantly y^4 dependence, as can be seen in the logarithmic plot in Figure 1-3.

To assess the impact on lens performance, consider a cylindrical lens for simplicity. One measure of the effect of aberrations of a lens is the Strehl ratio SR, which is the ratio of the peak far-field intensities with and without phase-front distortions. For uniform illumination of a cylindrical lens, the Strehl ratio is given by

$$SR = \left|\frac{1}{D}\int_{-D/2}^{D/2} e^{i2\pi\delta/\lambda} dy\right|^2 , \tag{1.6}$$

where D is the lens aperture and λ is the wavelength in air. The Strehl ratio is an indicator of the efficiency with which light is coupled into subsequent stages of an optical system, e.g., coupling into a fiber.

Equation (1.6) can be evaluated as a function of the numerical aperture with e as a parameter, as illustrated in the solid traces in Figure 1-4. Note that a Strehl ratio close to 1 is maintained for $\varepsilon = 0.02$, but severe degradation results at large numerical apertures when $\varepsilon = 0.1$. It should also be noted, however, that the Strehl ratio for $\varepsilon = 0.1$ can be considerably improved by fine adjustment of the source position for the introduction of an opposite wavefront curvature, as illustrated by the dashed traces in Figures 1-2 and 1-4. However, freedom for such adjustment may not always be available in some
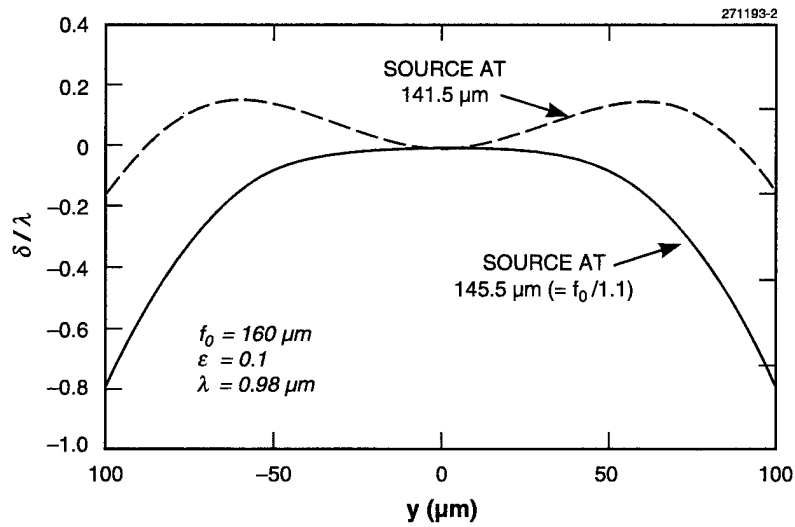
Figure 1-2. Phase distortions of mass-transport microlens that has been overetched by 10% in the fabrication of the lens preform. The parameter f_0 is the designed focal length of the microlens without the overetch.
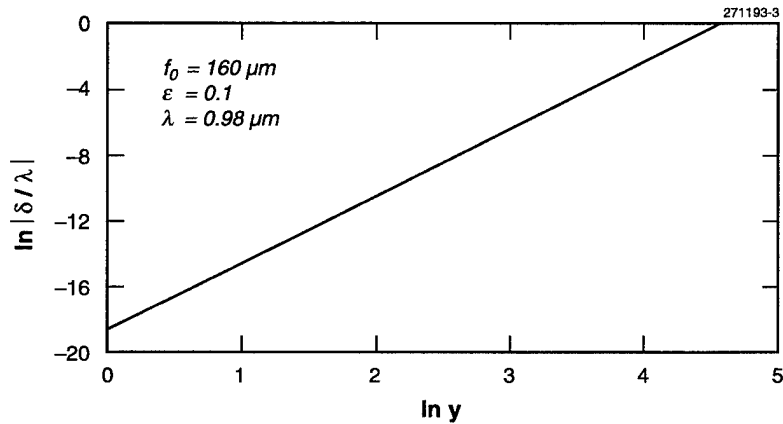
Figure 1-3. Logarithmic plot of phase distortion as a function of radial position resulting from 10% overetch of the lens preform (cf. the solid trace in Figure 1-2). This plot clearly shows a predominantly y^4 dependence of the phase deviation.

3
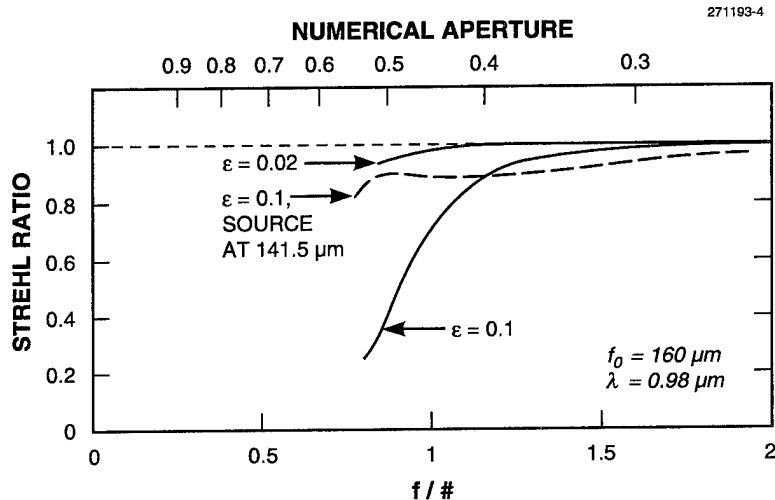
Figure 1-4. Calculated Strehl ratio in the case of uniform illumination for cylindrical mass-transport microlenses with two different overetches in the preform fabrication.

systems, such as anamorphic microlenses for astigmatism correction. Further, note that the Strehl ratio for a circular lens is more degraded (relative to a cylindrical lens) because the area weighting in the integral analogous to Equation (1.6) emphasizes the more distorted outer regions of the circular lens. Although this can also be analyzed, the following discussion will still be limited to cylindrical lenses for consistency.

For nonuniform lens illumination, the coupling efficiency between more general mode profiles can readily be shown to be

$$\eta = \frac{1}{N}\left|\int_{-D/2}^{D/2} \psi_B \, e^{i2\pi\delta/\lambda}\, \psi_A \, dy\right|^2 ,$$ (1.7)

where ψ_A is the amplitude profile of the incident beam after lens collimation, ψ_B is the amplitude profile of the mode to be coupled into, and N is the appropriate normalization factor. (Note that, in actual coupling of a laser mode to a single mode fiber or waveguide, an additional focusing lens or its equivalent is needed. The mode profiles in Equation (1.7) are those at the plane of the collimating lens.) By comparison with Equation (1.7), the Strehl ratio given by Equation (1.6) can be interpreted as the coupling efficiency between modes of uniform intensities. Conversely, Equation (1.7) can be considered as a weighted Strehl ratio for a nonuniformly illuminated lens.

4

For a case of practical interest, we now consider the coupling between two Gaussian modes of the same width, i.e.,

$$\eta = \left| \int_{-D/2}^{D/2} e^{i2\pi\delta/\lambda} e^{-2y^2/a^2} dy \right|^2 \bigg/ \left| \int_{-\infty}^{\infty} e^{-2y^2/a^2} dy \right|^2 , \qquad (1.8)$$

where e^{-y^2/a^2} is the amplitude profile of the incident beam. Two rather typical diode laser output beam divergences of 38 and 28° full width at half-intensity maximum, with corresponding a's of 90 and 66 μm, respectively, are used for the calculation shown in Figure 1-5. The coupling efficiencies start at low values for small numerical apertures because the incident light is not fully captured. As the numerical aperture increases, the efficiencies increase and become higher than those of the uniformly illuminated lenses because of less contribution from the more distorted outer regions.
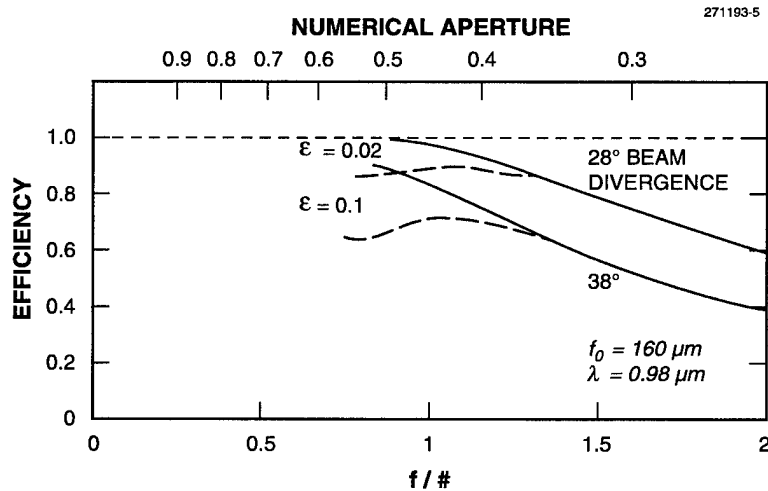
Figure 1-5. Calculated coupling efficiency in the case of a beam with Gaussian profile in one dimension incident on cylindrical mass-transport microlenses with two different preform overetches and two different incident beam divergences.

The present technique is rather generally applicable to other types of aberrations and is, in fact, not limited to microlenses. As an example, we have carried out calculations for aberrations resulting from small misalignment in the y-direction (i.e., with the source slightly off-axis) of a uniformly illuminated cylindrical lens, as shown in Figure 1-6. Note that the problem is more severe for lenses made of lower-index material. It is also worth noting that tolerances greatly improve by using the alternate lens configuration [5] as shown in Figure 1-7.

Z. L. Liau

5
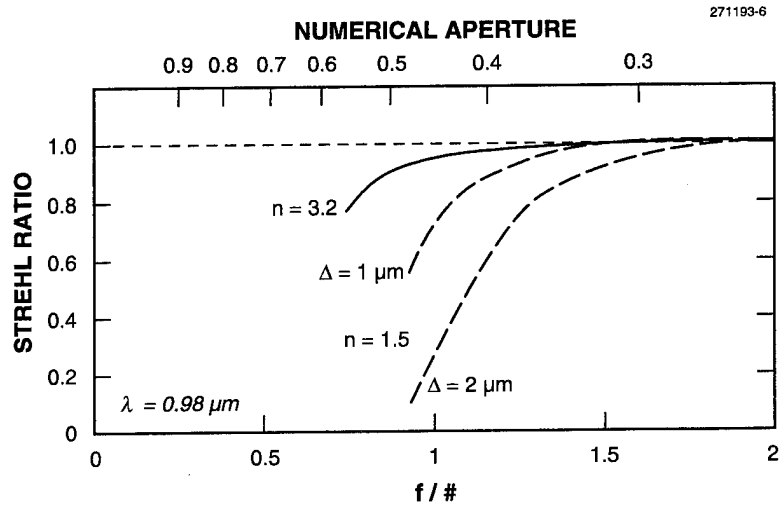
Figure 1-6 . Calculated Strehl ratios for slight misalignment of the source off the optical axis of uniformly illuminated cylindrical lens. The calculation has been carried out for two different misalignments and for lenses of different refractive indices.
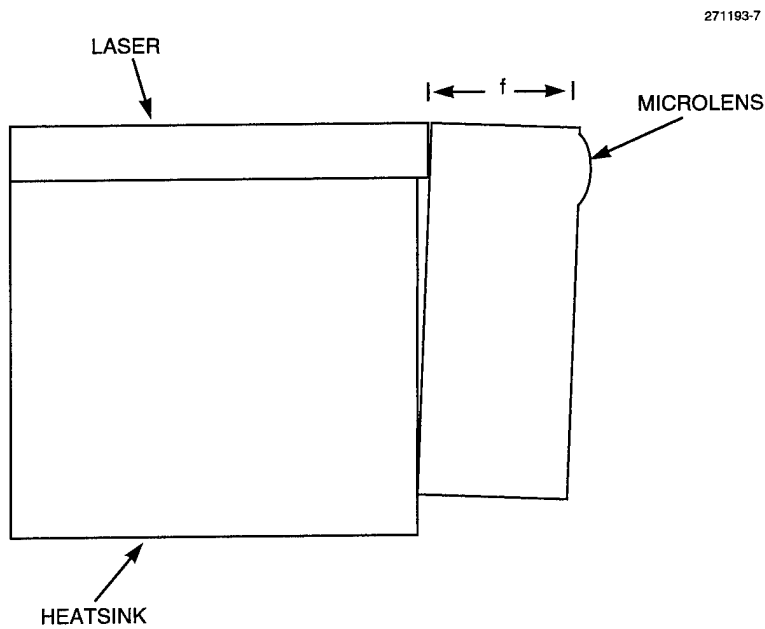
Figure 1-7. Alternative lens configuration that offers superior tolerances for lens and alignment accuracies.

6

REFERENCES

1. See, for example, M. E. Motamedi and L. Beiser, eds., *Micro-Optics/Micromechanics and Laser Scanning and Shaping*, Vol. 2383 of *Proc. SPIE* (1995).

2. Z. L. Liau, D. E. Mull, C. L. Dennis, R. C. Williamson, and R. G. Waarts, *Appl. Phys. Lett.* **64**, 1484 (1994).

3. Z. L. Liau, J. N. Walpole, D. E. Mull, C. L. Dennis, and L. J. Missaggia, *Appl. Phys. Lett.* **64**, 3368 (1994).

4. J. S. Swenson, Jr., R. A. Fields, and M. H. Abraham, *Appl. Phys. Lett.* **66**, 1304 (1995).

5. *Solid State Research Report*, Lincoln Laboratory, MIT, 1995:3, p. 1.

2. QUANTUM ELECTRONICS

2.1 PASSIVELY Q-SWITCHED MICROCHIP LASERS FOR ULTRAVIOLET GENERATION

Experimental studies of passively Q-switched picosecond microchip lasers [1] and the fourth-harmonic conversion of the output of these devices into the ultraviolet (UV) have been described previously [2]. Since these reports, we have generated the third and fifth harmonic of the microchip laser output, performed further characterization of the device, and worked out the theory of harmonic frequency conversion. These advances are discussed here, following a brief review of the previously reported work.

The principle behind the operation of a passively Q-switched laser is that the presence of a saturable absorber within the laser cavity prevents the onset of lasing until the average inversion density within the cavity reaches a critical value. The onset of lasing, at that point, produces a high intracavity optical field which quickly bleaches the saturable absorber, increasing the Q of the cavity and resulting in a Q-switched output pulse. The short cavity length of a microchip laser results in short optical pulses, and an infrared passively Q-switched Nd:YAG/Cr:YAG microchip laser, pumped by a fiber-coupled 1-W CW diode laser, has produced pulses as short as 218 ps (full width at half-maximum [FWHM]) with peak powers up to 25 kW and ideal beam quality (diffraction-limited TEM_{00} transverse mode, transform-limited single longitudinal mode, linearly polarized). It is the high peak power and ideal beam quality of the passively Q-switched infrared microchip laser that allows for efficient frequency conversion to the visible and UV regions of the spectrum using nonlinear optical crystals.

The Q-switched microchip laser used for the harmonic generation discussed below had a total cavity length of 1.25 mm, comprising 1 mm of Nd^{3+}:YAG and 0.25 mm of Cr^{4+}:YAG, and an output coupler with 85% reflectivity. It generated 8-μJ, 440-ps pulses at a repetition rate of 10 kHz. The output at 1.064 μm was single frequency and diffraction limited, with a 6.8-mrad single-sided divergence and a $1/e^2$ waist diameter of 100 μm. Although we have constructed passively Q-switched microchip lasers with higher peak powers, this device had a combination of peak power and waist size (and hence confocal parameter) that were well matched to the requirements for efficient UV generation in the desired compact format without any intermediate optics.

The 1.064-μm radiation from this microchip laser was frequency doubled with 44% energy efficiency in a 5-mm-long crystal of KTP placed adjacent to the laser (with no intervening optics) and oriented for type II phase matching. The 532-nm output had a circularly symmetric, nearly Gaussian (super-Gaussian) profile with a 5.9-mrad divergence and an 85-μm waist diameter. The 3.5-μJ green pulses had a duration of 380 ps.

To generate the UV harmonics of the microchip laser output, we used antireflection-coated pieces of β-BaB$_2$O$_4$ (BBO) oriented for type I phase matching. In all cases, the crystals were 5 mm long, had flat faces, and were placed in the output path of the laser with no intervening optics. Before discussing the experimental UV generation, we will briefly review the theory of harmonic generation in BBO, in the limit of low conversion efficiency.

9

BBO has significant double refraction. For third-, fourth-, or fifth-harmonic generation of the output of the Nd:YAG microchip laser, the harmonically generated beam walks out of the aperture defined by the generating beams in a length that is short compared to the length l of BBO used. The aperture length for coherent interaction of the beams is [3]

$$l_a = \frac{\sqrt{\pi}\omega_{e3}}{\tan(\rho_3)} \, ,$$

(2.1)

where

$$\omega_{e3} \approx \left[\frac{1}{\omega_{e1}^2} + \frac{1}{\omega_{e2}^2} \right]^{-1/2} \, ,$$

(2.2)

in which ω is the $1/e^2$ radius of a nearly Gaussian beam, the subscripts 1, 2, and 3 refer to the generating and generated beams, respectively, and the subscript e indicates that the waist dimensions are measured in the direction perpendicular to the ordinary optic axis of the crystal (o indicates the direction parallel to the ordinary axis); and where the walk-off angle ρ_3 is given by

$$\tan(\rho_3) = \frac{\left[\frac{n_{o3}^2}{n_{e3}^2} - 1 \right] \tan\theta}{1 + \frac{n_{o3}^2}{n_{e3}^2} \tan^2\theta} \, ,$$

(2.3)

in which n_{o3} and n_{e3} are the ordinary and extraordinary refractive indices at the frequency of the generated beam and θ is the phase-matching angle in the crystal defined by

$$\Delta k = 2\pi \left[\frac{n_{e3}(\theta)}{\lambda_3} - \frac{n_{o2}}{\lambda_2} - \frac{n_{o1}}{\lambda_1} \right] = 0 \, ,$$

(2.4)

with λ being the free-space wavelength and

$$n_{e3}(\theta) = \left[\frac{\cos^2\theta}{n_{o3}^2} + \frac{\sin^2\theta}{n_{e3}^2} \right]^{-1/2} \, .$$

(2.5)

The peak intensity of the generated beam is given by

$$I_3 = \frac{2\pi^2 d_{\text{eff}}^2}{n_{o1}n_{o2}n_{e3}(\theta)c\varepsilon\lambda_3^2} f(\delta\theta_1)f(\delta\theta_2)l_a^2 I_1 I_2 \, ,$$

(2.6)

10

where

$$d_{\text{eff}} = d_{31}\sin(\theta + \rho_3) - d_{22}\cos(\theta + \rho_3)\sin 3\phi \tag{2.7}$$

is the effective nonlinear coefficient ($\phi = 90°$ for a properly oriented crystal), c is the speed of light, ε is the dielectric constant of free space, and $f(\delta\theta) \leq 1$ is a function of the amount of power in one of the generating beams that falls within the acceptance angle of the crystal. When the acceptance angle of the crystal

$$\theta_{\text{acc}} = \frac{2\pi}{l_a}\left[\frac{\partial \Delta k}{\partial \theta}\right]^{-1} \tag{2.8}$$

is smaller than the divergence angle θ_e (in the BBO) of a generating beam, we will use

$$f(\delta\theta) \approx \frac{\theta_{\text{acc}}}{\theta_e} \; . \tag{2.9}$$

For all calculations, we will assume $|d_{31}| \ll |d_{22}|$, $|d_{22}| = 2.2$ pm/V [4], and the refractive indices given in Table 2-1 [5].

TABLE 2-1

Refractive Indices of β-BaB$_2$O$_4$ at Nd:YAG Harmonics

λ (nm)	n_o	n_e
1064	1.54254	1.65510
532	1.55552	1.67493
355	1.57757	1.70556
266	1.61461	1.75707
213	1.67467	1.84707

The peak power P_3 and pulse energy E_3 in the generated beam are calculated from the peak intensity. In the dimension parallel to the ordinary axis of the BBO, we will assume that the generated beam has a nearly Gaussian profile with a $1/e^2$ radius of ω_{o3}. In the orthogonal dimension, the direction of walk-off, the profile is roughly top hat, with a diameter

$$d_3 = \frac{l}{\tan(\rho_3)} \; . \tag{2.10}$$

The peak power is approximately

$$P_3 = \frac{\sqrt{2}I_3}{\sqrt{\pi}\omega_{o3}d_3}$$

(2.11)

and, after accounting for the temporal shape of the pulse, the pulse energy is approximated by [6]

$$E_3 = 1.16 P_3 t_3 \; ,$$

(2.12)

where a reasonable estimate of the pulse duration (FWHM) is

$$t_3 = \left[\frac{1}{t_1^2} + \frac{1}{t_2^2}\right]^{-1/2} .$$

(2.13)

The green output of the KTP was doubled to produce 266-nm UV radiation with 20% energy efficiency in a 5-mm-long crystal of BBO placed adjacent to the KTP. The far-field profile of the resulting 0.7-μJ UV pulses was nearly Gaussian in the dimension parallel to the ordinary axis of the BBO, with a $1/e^2$ single-sided divergence of 4.1 mrad. In the opposite dimension the far-field profile approximated a $\sin^2 x/x^2$ pattern, with an angular separation of 1.1 mrad between the two central nodes. The near-field and temporal profiles of the UV output were not measured.

From the theory presented above, for fourth-harmonic generation of the microchip output $\theta = 47.3°$, $\rho_3 = -4.84°$, $|d_{\text{eff}}| = 1.62$ pm/V, $\omega_{o3} = 30 \; \mu$m, $d_3 = 423 \; \mu$m, $t_3 = 269$ ps, $l_a = 627 \; \mu$m, $n_{e3}(\theta) = 1.687$, and $f(\delta\theta_1) = f(\delta\theta_2) = 0.91$. With $I_1 = I_2 = 287$ MW/cm^2 ($I_1 = \pi\omega_1^2 P_1/2$), this gives calculated values of $I_3 = 17.9$ MW/cm^2, $P_3 = 2844$ W, and $E_3 = 0.89 \; \mu$J; in excellent agreement with the 0.7 μJ obtained. From the theoretical calculations, the far-field divergence of a diffraction-limited beam in the direction parallel to the ordinary axis would be 2.8 mrad, indicating that the actual beam was ~1.4 times diffraction limited, similar to the 532-nm generating beam. In the opposite dimension, the far-field profile of a 423-μm-diam top hat should have central nulls spaced by 1.2 mrad, in good agreement with the observed value.

To generate the third harmonic of the 1.064-μm microchip output, the fundamental frequency was combined with the second harmonic in a properly oriented BBO crystal placed adjacent to the KTP. When the KTP was oriented for maximum 532-nm generation, the output energy at 355 nm was 0.24 μJ/pulse. The output was increased to 0.3 μJ/pulse by rotating the KTP in the plane normal to the propagation of the 1.064-μm radiation. The far-field profile of the 355-nm output (under conditions of maximum output energy) was qualitatively similar to that obtained at 266 nm, with a $1/e^2$ divergence of 3 mrad in the nearly Gaussian dimension, and a central node spacing of 1.0 mrad in the orthogonal dimension.

When the KTP was oriented for maximum 532-nm generation, the peak intensity of the infrared remaining after the doubling crystal was 112 MW/cm^2 [I(1.064 μm) – I(532 nm)]. However, as a result of the type II phase matching in the KTP, only half of this was properly polarized to contribute to third-harmonic generation in type I phase-matched BBO, with the result that $I_1 = 56$ MW/cm^2 and $I_2 = 287$ MW/cm^2. Under these conditions, the calculated pulse energy at 355 nm is 0.26 μJ (to be compared with

the measured value of 0.24 μJ). By properly rotating the KTP, the intensities of the first- and second-harmonic radiation are brought into balance, while the fraction of the first harmonic that is properly polarized for third-harmonic generation is increased. As a result, the amount of third harmonic generated was increased by 25%.

The 266-nm radiation was also combined with the fundamental to generate 213-nm light in a properly oriented crystal of BBO placed adjacent to the frequency-quadrupling crystal. When aligned for maximum output energy, the ordinary axis of the fifth-harmonic crystal was perpendicular to the ordinary axis of the fourth-harmonic crystal, and fifth-harmonic pulse energies of ~ 0.01 μJ were obtained. (Because of the low average power at this wavelength, the uncertainty in the energy measurement is ~ 50%.) The far-field profile of the 213-nm output was qualitatively similar to that of the 266-nm light, except rotated by 90° due to the relative orientations of the fourth- and fifth-harmonic crystals. The $1/e^2$ divergence in the nearly Gaussian dimension was ~ 1.5 mrad, and the central node spacing in the other dimension was 0.8 mrad.

As in the case of third-harmonic generation, only half of fundamental remaining after second-harmonic generation in the KTP is properly polarized to contribute to fifth-harmonic generation. In this case, the useful 1.064-μm radiation is polarized perpendicular to the ordinary axis of the BBO crystal used for fourth-harmonic generation, and experiences double refraction in that crystal, with a "walk-off" angle of –4.03°. As a result, it overlaps the fourth-harmonic radiation at a position of uniform, maximum intensity. If we ignore the divergence of the 1.064-μm radiation, the theory presented above predicts a pulse energy of 0.01 μJ. At the position of the fifth-harmonic crystal, the fundamental beam should have diverged by 40% in radius, decreasing the amount of generated fifth harmonic proportionally.

We also built a single device that simultaneously generated the first five harmonics of Nd:YAG. This was done by positioning a third-harmonic crystal immediately after the KTP, after the fourth-harmonic crystal, or after the fifth-harmonic crystal. Different positions of the third-harmonic crystal resulted in different output powers at each of the UV wavelengths.

The most thoroughly tested of the devices discussed above is a frequency-quadrupled passively Q-switched microchip laser. The laser and the nonlinear crystals are packaged in a stainless-steel cylinder 1 cm in diameter by 3 cm in length [2]. As a result of the short aperture length (l_a) in the BBO, the temperature window for UV generation is large and at least 1 mW of time-averaged UV output is obtained over a temperature range from 0 to 70°C. Currently, this device has been operated for > 10^{10} shots without degradation.

The use of 5-mm-long crystals of BBO in all of the experiments described above is somewhat arbitrary. When the aperture length in the nonlinear crystal is short compared to the crystal length, as is the case here, the conversion efficiency is linearly dependent on the crystal length, to the extent that pump depletion and beam divergence can be neglected. The amount of UV generated at any of the Nd:YAG harmonics could be increased simply by using a longer piece of BBO. Since the acceptance angle and temperature window for nonlinear conversion are determined by the aperture length, they are not affected.

J. J. Zayhowski   C. Cook
C. Dill III   J. L. Daneu
J. Ochoa

13

REFERENCES

1. *Solid State Research Report,* Lincoln Laboratory, MIT, 1994:2, p. 13; J. J. Zayhowski and C. Dill III, *Opt. Lett.* **18**, 1427 (1994).

2. *Solid State Research Report,* Lincoln Laboratory, MIT, 1995:1, p. 7; J. J. Zayhowski, J. Ochoa, and C. Dill III, *Conference on Lasers and Electro-Optics Technical Digest,* Vol. 15 (Optical Society of America, Washington, D.C., 1995), Paper CTuM2.

3. G. D. Boyd, A. Ashkin, J. M. Dziedzic, and D. A. Kleinman, *Phys. Rev. A* **137**, 1305 (1965).

4. R. C. Eckardt, H. Masuda, Y. X. Fan, and R. L. Byer, *IEEE J. Quantum Electron.* **26**, 922 (1990).

5. D. Eimerl, L. Davis, S. Velsko, E. K. Graham, and A. Zalkin, *J. Appl. Phys.* **62**, 1968 (1987).

6. J. J. Zayhowski and P. L. Kelley, *IEEE J. Quantum Electron.* **27**, 2220 (1991); **29**, 1239 (1993).

3. MATERIALS RESEARCH

3.1 HIGH THERMOELECTRIC FIGURES OF MERIT IN PbTe QUANTUM WELLS

Recent renewed efforts to improve thermoelectric cooling materials have stimulated considerable interest in the concept of creating multiple-quantum-well (MQW) superlattices to increase thermoelectric properties [1]. Calculations by Hicks and Dresselhaus [2] showed a very large increase in the two-dimensional (2D) thermoelectric figure of merit $Z_{2D}T$ of a single Bi_2Te_3 quantum well as the thickness of the well decreased, because of the large density of states per unit volume that occurs for small well widths. Here, we report a first-of-its-kind investigation of the thermoelectric properties of $Pb_{1-x}Eu_xTe/$ PbTe MQW structures grown by molecular beam epitaxy (MBE) on BaF_2 substrates, where enhanced thermoelectric properties are also anticipated via the same effect. The PbEu-chalcogenide material system is well suited for investigating thermoelectric properties of quantum wells, because it is both a good thermoelectric material [3] and, unlike Bi_2Te_3, has a good epitaxial growth technology base [4]–[6].

The figure of merit for a thermoelectric material is given by

$$ZT = S^2\sigma T/\kappa = P_F T/\kappa \quad , \tag{3.1}$$

where S, σ, κ, T, and P_F ($= S^2\sigma$) are the Seebeck coefficient, the electrical conductivity, the thermal conductivity, the temperature, and the thermoelectric power factor, respectively. High P_F and low κ are desirable to obtain the highest possible ZT for efficient cooling and energy conversion applications. For homogeneous material, Equation (3.1) can also be written as

$$ZT = S^2 ne\mu T/(\kappa_l + \kappa_e) \quad , \tag{3.2}$$

where n, e, μ, κ_l, and κ_e are the carrier density, electronic charge, carrier mobility, and the lattice and electronic parts of the thermal conductivity, respectively. The electronic part of the thermal conductivity in Equation (3.2) is determined from the Wiedemann-Franz law as

$$\kappa_e = L_o \sigma \quad , \tag{3.3}$$

where L_o is a parameter dependent on the electron scattering mechanism and the statistics [7]. Here, we used $L_o = 4.4 \times 10^{-6} \ \Omega$ W/K. For PbTe we used $\kappa_l = 20$ mW/cm K [8].

In the case of an MQW structure, if we assume that current and heat flow only through the quantum wells, we get a 2D thermoelectric figure of merit

$$Z_{2D}T = S^2 n_w e\mu T/(\kappa_l^w + \kappa_e^w) \quad , \tag{3.4}$$

where n_w, κ_l^w, and κ_e^w are the carrier density and lattice and electronic parts of the thermal conductivity of the quantum wells, respectively. The 2D power factor is likewise given by

15

$$P_{F2D} = S^2 \sigma_w = S^2 n_w e \mu \quad , \qquad\qquad (3.5)$$

where σ_w is the electrical conductivity of the quantum wells.

The MBE growth was carried out on 1.8 × 1.8-cm, as-received, cleaved BaF_2 (111) substrates with thicknesses of ~ 1 mm, which were thermally cleaned in the MBE system at 490°C for 32 min prior to growth of a $Pb_{0.958}Eu_{0.042}Te$ buffer layer at 350°C. Reflection high-energy electron diffraction (RHEED) patterns indicated a change in growth morphology from 3D islands to 2D layer-by-layer growth and a smooth surface for subsequent MQW structure growth. Buffer-layer growth was then continued an additional 8 min for a total thickness in the range 1100–1900 Å. Since the accuracy of the measured thermoelectric properties improves with film thickness, relatively thick MQW structures in the range 4.5–6 μm were grown at about 300°C with the number of periods typically equal to 120. Growth rates were in the range 0.75–1.0 μm/h. Effusion cells containing Eu, zone-refined PbTe [9], and Te_2 were used in growing the undoped $Pb_{0.958}Eu_{0.042}Te$ buffer layers. Only one effusion cell containing zone-refined PbTe was used for the quantum-well growth, but four effusion cells were used for the Bi-doped $Pb_{0.927}Eu_{0.073}Te$ barriers, i.e., PbTe, Eu, Te_2, and Bi. Good-quality RHEED streaks were observed throughout the growth of the MQWs indicating high-quality 2D growth for the entire structure.

A schematic cross section of the $Pb_{0.927}Eu_{0.073}Te/PbTe$ MQW structure along with the $Pb_{0.958}Eu_{0.042}Te$ buffer layer and the BaF_2 substrate is shown in Figure 3-1. Thin, undoped buffer layers were used so that the electrical conductance of the buffer layer would be negligible relative to the conductance of the approximately 120 quantum wells in each film. The electrical conductance and

271193-8

PbTe
$Pb_{1-x}Eu_xTe$
PbTe
$Pb_{1-x}Eu_xTe$
PbTe

| PbTe |
|---|
| $Pb_{1-x}Eu_xTe$ |
| PbTe |
| $Pb_{1-y}Eu_yTe$ |
| BaF_2 SUBSTRATE |

d_b

d_w

GROWTH DIRECTION
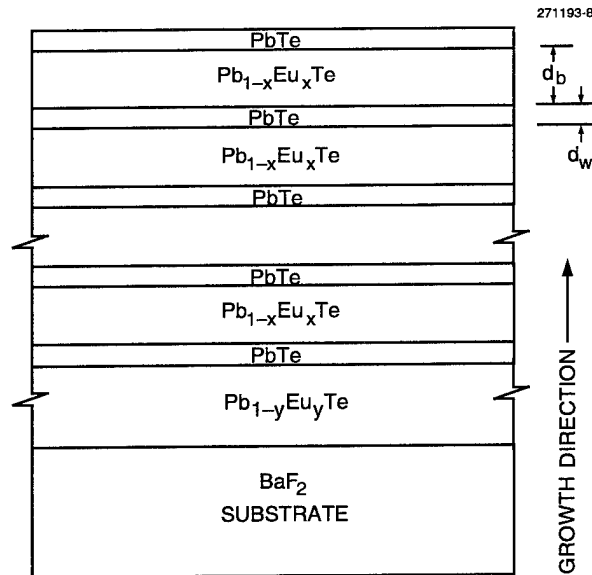
Figure 3-1. Schematic cross section of the PbEu-chalcogenide multiple-quantum-well structure investigated.

16

Seebeck coefficients of the MQW structures were measured with the temperature gradient and electric field applied parallel to the epilayer interfaces. Theoretical calculations by Hicks and Dresselhaus [10] indicate that the electrical conduction through the barrier layers is negligible compared to that through the quantum-well layers for the MQW structures used in the experiments reported here. Also, the conductance of the thin, low-doped, low-carrier-mobility $Pb_{1-y}Eu_yTe$ buffer layer was negligible. Numerous $Pb_{1-x}Eu_xTe/PbTe$ MQW samples were grown with PbTe well widths in the range 10–50 Å and $Pb_{1-x}Eu_xTe$ barrier widths in the range 300–600 Å. Samples with $x = 0.042$ exhibited a large decrease in electron mobility with increasing barrier width, indicative of 3D conduction. For the case of 26-Å wells and 1300-Å barriers, the 300-K carrier mobility for a carrier density of $\sim 10^{17}$ cm^{-3} (averaged over the well and barrier) was only 240 cm^2/V s, which is very close to the electron mobility of $Pb_{0.958}Eu_{0.042}Te$.

For $Pb_{0.927}Eu_{0.073}Te/PbTe$ MQW samples, we found high electron mobilities at large barrier thickness, confirming our expectations of 2D conduction for these wide barriers. To investigate the theoretical predictions [2],[10], various $Pb_{0.927}Eu_{0.073}Te/PbTe$ MQW samples were grown with PbTe well widths in the range 15–50 Å and $Pb_{0.927}Eu_{0.073}Te$ barrier widths in the range 360–540 Å. The Eu content in the barriers was kept at $x = 0.073 \pm 0.004$, which gives a difference in band gap between the PbTe wells and the $Pb_{0.927}Eu_{0.073}Te$ barriers of ~ 0.4 eV at 300 K. The published works agree that a type I band alignment occurs for a $Pb_{1-x}Eu_xTe/PbTe$ superlattice in the range of compositions of x smaller than 0.10. Since for $x < 0.05$ the band offsets are nearly symmetric [11],[12], we would expect for $x = 0.073$ that the conduction band offset or barrier height is ~ 0.2 eV. Modulation-doped $Pb_{0.953}Eu_{0.047}Te/PbTe$ MQW samples with very wide barrier layers and low carrier concentrations have been shown to exhibit enhanced carrier mobilities at 77 K because of the spatial separation of electrons from their donors [5]. In modulation doping only the wide-gap barrier layer material is doped leaving the PbTe quantum-well layer relatively free of impurities. Electrons are transferred laterally from the donor states of the higher-lying conduction band edge of the $Pb_{0.927}Eu_{0.073}Te$ barriers to the lower conduction band states in the PbTe well layer. Thus, a spatial separation of electrons from the impurities occurs. All of our MQW samples were modulation Bi doped.

The measured thermoelectric parameters of the $Pb_{0.927}Eu_{0.073}Te/PbTe$ MQW samples, including carrier concentrations, carrier mobilities, Seebeck coefficients, and thermoelectric power factors, are given in Table 3-1. The Seebeck coefficients are also displayed in Figure 3-2 as a function of carrier concentration along with values for our single-layer PbTe films and numerous selected high-quality bulk n-type PbTe samples [13]. At low carrier concentrations the average 300-K carrier mobility for the bulk samples was 1600 cm^2/V s, which decreased to 940 cm^2/V s at a carrier concentration of 3.9×10^{19} cm^{-3}. The S vs n data for the bulk PbTe was fit by a straight line given by the simple expression

$$S \ (\mu V/K) = -477 + 175 \ \log_{10}(n/10^{17} \ cm^{-3}) \quad . \tag{3.6}$$

From this expression and the slow mobility change with carrier concentration, we get a maximum thermoelectric power factor of 38 μW/cm K^2 at $\sim 6 \times 10^{18}$ cm^{-3}, which is consistent with the best reported values for PbTe. Using $\kappa_l = 20$ mW/cm K, we calculate $ZT_{max} = 0.45$.

17

Our single-layer PbTe films had somewhat lower electron mobilities than high-quality bulk PbTe. This is presumably a result of unoptimized growth. However, one of our MQW samples had a very high mobility (1420 cm^2/V s)—higher than that of our single-layer PbTe films and at least equal to the mobility for the best bulk PbTe samples. That this is achieved when the MQW film is composed mostly (95%) of very low mobility (45 cm^2/V s at 300 K) $Pb_{0.927}Eu_{0.073}Te$ material is strong evidence that pure 2D conduction is occurring and that modulation doping can be effective in these $Pb_{0.927}Eu_{0.073}Te/PbTe$ MQW samples with nearly optimized growth conditions. There is a wide variation in the carrier mobility from the best sample to the worst, and it is believed that mobility is quite sensitive to the growth variables such as effusion cell flux ratios. In general, our $Pb_{0.927}Eu_{0.073}Te/PbTe$ MQW films have somewhat lower electron mobilities than the single-layer PbTe films, although 20× higher than that of the $Pb_{0.927}Eu_{0.073}Te$ barrier material. No focused effort was applied to optimization of the epitaxial growth.

TABLE 3-1

Thermoelectric Properties of $Pb_{0.927}Eu_{0.073}Te/PbTe$ Multiple-Quantum-Well Structures

Sample No.	Thickness of PbTe Wells (Å)	Carrier Concentration (cm^{-3})	Carrier Mobility (cm^2/V s)	Seebeck Coefficient (μV/K)	2D Power Factor P_{F2D} (mV/cm K^2)	Calculated Figure of Merit $Z_{2D}T$
T-225	19	1.1×10^{19}	1420	−225	130	1.23
T-229	20	1.1×10^{19}	710	−235	66	0.78
T-235	23	5.9×10^{18}	650	−303	55	0.73
T-246	15.5	7.5×10^{18}	1050	−222	62	0.72
T-236	23	6.7×10^{18}	640	−282	54	0.71
T-218	45	4.8×10^{18}	950	−174	22	0.29
T-222	34	4.8×10^{18}	890	−166	19	0.24
T-208	40	3.7×10^{18}	800	−188	17	0.23
T-215	41	5.1×10^{18}	850	−157	17	0.22

The Seebeck coefficient values of our PbTe epilayers are equivalent to values of the bulk PbTe and nicely fill in the data gap in Figure 3-2 near 6×10^{18} cm^{-3}. The Seebeck coefficient values of the MQW films show a decrease with increasing carrier concentration similar to that of bulk material. In the theoretical calculations [2],[10] of $Z_{2D}T$, carrier mobility and thermal conductivity in the quantum wells were assumed equal to bulk values and independent of well thickness. Thus, from Equation (3.4) we need only examine S^2n, and since S varies with n, we can simply compare quantum-well S values with bulk
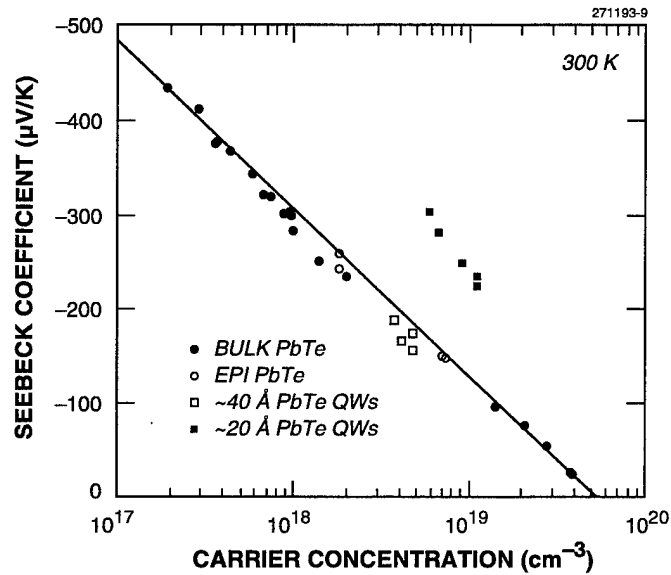
Figure 3-2. Seebeck coefficient vs carrier concentration for n-type bulk PbTe, epitaxial PbTe, and $Pb_{0.927}Eu_{0.073}Te/PbTe$ quantum wells.

values near the optimum carrier concentration ($\sim 6 \times 10^{18}$ cm^{-3}). Note that the samples with $\sim$ 40-Å well widths have S values very close to the bulk curve. As the well width was decreased S increased, and at well widths near 20 Å, we obtained Seebeck coefficients about 2× higher than those obtained with high-quality bulk material. This rapid increase with decreasing well width is in agreement with the calculations [2],[10]. Well widths thinner than 17 Å did not result in improvements, possibly because of interface effects or because 2D conduction is no longer achieved. The thickness of these thin wells corresponds to only four to six atom layers or two to three molecular layers.

The thermoelectric power factors ($S^2\sigma$ and $S^2\sigma_w$) are presented in Figure 3-3 as a function of the carrier concentration at 300 K. The dotted curve was calculated by fitting the bulk Seebeck coefficient and mobility data, and provides information near the optimum bulk carrier concentration of $\sim 6 \times 10^{18}$ cm^{-3}, where $S^2\sigma \approx 38$ μW/cm K^2 is expected. Because of slightly lower electron mobilities, the power factors for our single-layer PbTe films are below the bulk PbTe curve. The 2D power factors $S^2\sigma_w$ for thick-quantum-well films are somewhat further below the bulk PbTe curve, mainly because of low mobility. However, for the thin PbTe quantum wells, significantly higher 2D power factors are seen despite their generally lower mobilities. For the one high-mobility sample T-225 the power factor is 130 μW/cm K^2, the highest reported to date for good thermoelectric materials.
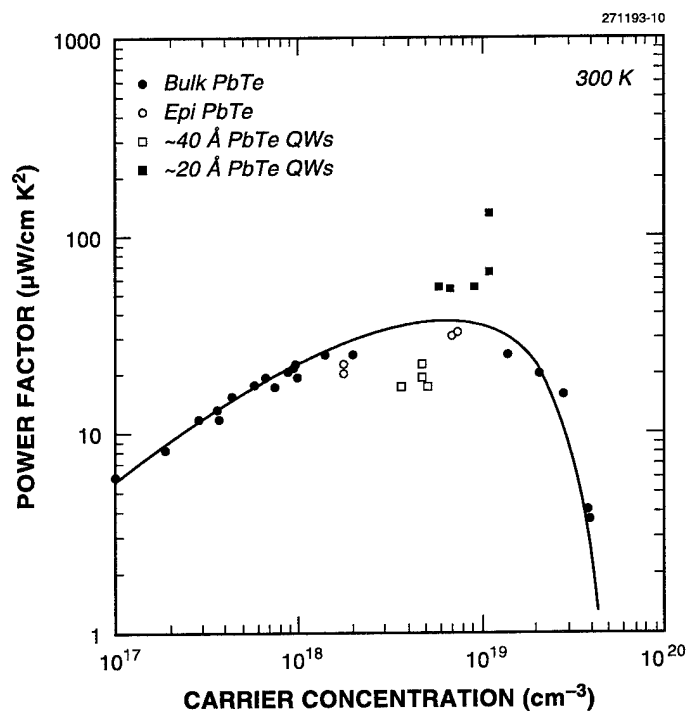
Figure 3-3. *Thermoelectric power factor vs carrier concentration for n-type bulk PbTe, epitaxial PbTe, and* $Pb_{0.927}Eu_{0.073}Te/PbTe$ *quantum wells.*

The 2D figures of merit for the PbTe quantum wells shown in Table 3-1 were calculated using Equations (3.3) and (3.4). For all five narrow-quantum-well samples, $Z_{2D}T$ exceeded the expected ZT_{max} = 0.45 of bulk PbTe. For sample T-225, the combined enhancement of the Seebeck coefficient and mobility resulted in $Z_{2D}T$ = 1.23, a result that breaks the decades-old $ZT \cong 1.0$ barrier for thermoelectric materials at 300 K. These results establish the proof of principle of an enhanced ZT at 300 K in thermo-electric quantum wells, presumably because of the large density of states per unit volume increase that occurs for small well widths in a quasi-2D geometry. Seebeck coefficients are 2× larger than those of high-quality bulk PbTe for quantum-well widths in the range 17–23 Å. The combined enhancements of the Seebeck coefficient and mobility resulted in an increase in the 300-K ZT of PbTe from ~ 0.45 for bulk material to $Z_{2D}T$ > 1.2 in the best quantum wells. Although much remains to be done, as the best overall or 3D ZT of these MQW structures was only 0.11, this work represents a first step toward the goal of achieving materials with 3D ZT > 1.0.

T. C. Harman   R. E. Fahey
D. L. Spears   M. P. Walsh
M. J. Manfra

20

REFERENCES

1. T. C. Harman, U.S. Patent No. 5,415,699 (16 May 1995).

2. L. D. Hicks and M. S. Dresselhaus, *Phys. Rev. B* **47**, 12727 (1993).

3. See, for example, F. D. Rosi, *Solid-State Electron.* **11**, 833 (1968).

4. D. L. Partin, *IEEE J. Quantum Electron.* **24**, 1716 (1988).

5. G. Springholz, G. Ihninger, G. Bauer, M. M. Olver, J. Z. Pastalan, S. Romaine, and B. B. Goldberg, *Appl. Phys. Lett.* **63**, 2908 (1993); G. Springholz and G. Bauer, *Appl. Phys. Lett.* **60**, 1600 (1992); G. Springholz, G. Bauer, and G. Ihninger, *J. Cryst. Growth* **127**, 302 (1993).

6. M. M. Olver, J. Z. Pastalan, S. E. Romaine, B. B. Goldberg, G. Springholz, G. Ihninger, and G. Bauer, *Solid State Commun.* **89**, 693 (1994); S. Yuan, G. Springholz, G. Bauer, and M. Kriechbaum, *Phys. Rev. B* **49**, 5476 (1994); personal communication from G. Bauer.

7. See, for example, T. C. Harman and J. M. Honig, *Thermoelectric and Thermomagnetic Effects and Applications* (McGraw-Hill, New York, 1967), and references therein.

8. See, for example, G. Nimtz and B. Schlicht, *Narrow-Gap Semiconductors*, Vol. 98 of *Springer Tracts in Modern Physics* (Springer, Berlin, 1983), and references therein.

9. T. C. Harman, *J. Nonmetals* **1**, 183 (1973).

10. L. D. Hicks and M. S. Dresselhaus, private communication.

11. A. Ishida, S. Matsuura, M. Mizuno, and H. Fujiyasu, *Appl. Phys. Lett.* **51**, 478 (1987).

12. S. Yaun, H. Krenn, G. Springholz, and G. Bauer, *Appl. Phys. Lett.* **62**, 885 (1993).

13. A. J. Strauss, private communication; *J. Electron. Mater.* **2**, 553 (1973).

4. SUBMICROMETER TECHNOLOGY

4.1 PLASMA-DEPOSITED SILYLATION RESIST FOR 193-nm LITHOGRAPHY

Dry-deposited, dry-developed photoresists hold numerous potential advantages over conventionally synthesized spin-applied, wet-developed photoresists. All-dry resists enable lithography on materials that may react with solvents or liquid developers, those which require minimal handling, or those prone to contamination or oxidation. Photoresists deposited by plasma-enhanced chemical vapor deposition (PECVD) can be used on any size or shape substrate, over varying degrees of topography, and permit process flexibility through in-situ synthesis tailored to a specific application. They also avoid costly waste and disposal problems associated with conventional spin-on resists. Our initial work on negative-tone PECVD organosilicon thin films for 193-nm lithography [1] and more recent work by Wiedman and Joshi [2] on organosilicon imaging layers for mid-ultraviolet lithography show the potential viability of all-dry photoresist.

Plasma-deposited photoresist synthesis has different constraints than conventional polymer synthesis. An advantage is that the desired chemical properties of the polymer are not limited by the precursor materials but can be created through plasma synthesis. A drawback to this synthesis method is that as a single-wafer process, reproducibility is essential. Also, the deposition rate must be at least on the order of 0.3 μm/min. In addition, plasma polymerization has sharply unstable regimes with respect to deposition of uniform, particle-free polymer films. Deposition variables such as precursor ratios, flow rates, deposition pressure, power, electrode spacing (geometry of reactor), and temperature must be carefully optimized to avoid gas-phase polymerization or highly nonuniform deposition.

In our experiments, all films were deposited from liquid hydrocarbon precursors and oxygen-based gases in a conventional 13.56-MHz RF-powered parallel-plate reactor. Gases were introduced through a water-cooled shower head in the top electrode at flow rates from 1 to 400 sccm. Films were deposited at relatively high pressures (300–3000 mTorr) and various RF powers (50–400 W) onto 4-in. wafers robotically loaded onto the bottom, temperature-controlled (powered) electrode. A variety of techniques, including ultraviolet-visible spectroscopy, Fourier transform infrared spectroscopy (FTIR), thermal-mechanical analysis (TMA), and ellipsometry were used to characterize the photoresist. Patterned exposures were performed using Lincoln Laboratory's 0.35-numerical-aperture modified 193-nm GCA 10× stepper. Samples were silylated using dimethylsilyldimethylamine (DMSDMA) at 10 Torr for various times and temperatures in a computer-controlled silylation system. Pattern transfer was performed with oxygen plasmas both in a conventional reactive ion etching system at –200-V self-bias and in a high-ion-density helicon reactor.

Our benchmark in developing an all-dry positive-tone silylation resist for 193-nm lithography is spin-applied polyvinylphenol, also known as polyhydroxystyrene (PHOST). We began plasma synthesis by depositing films from high-vapor-pressure unsaturated cyclic hydrocarbon precursors and oxygen-based gases, since no volatile aromatic compounds containing hydroxyl groups are available as precursors to synthesize a chemical analog to PHOST using PECVD. Figure 4-1 shows the FTIR spectrum of a film deposited from benzene and oxygen and for comparison the spectrum of an equal thickness film of
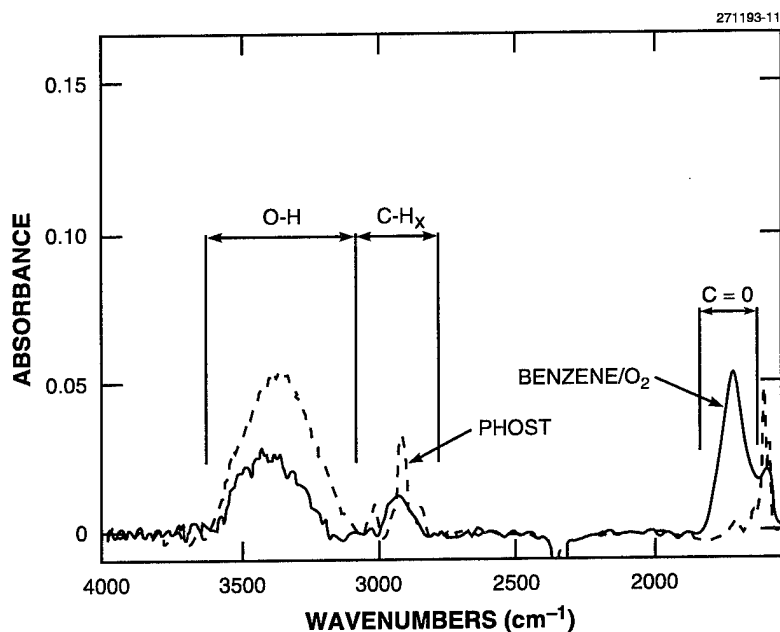
Figure 4-1. Fourier transform infrared spectroscopy (FTIR) absorbance spectra of polyhydroxystyrene and a film deposited from benzene and oxygen. The bands are identified, which are signatures of the O-H, C-H$_x$, and C=O moieties.

PHOST. Note that both films have a characteristic broad hydroxyl peak centered around 3400 cm^{-1} and both have an aliphatic C-H$_x$ stretch centered around 2950 cm^{-1} and aromatic-related peaks at 1600 and 3050 cm^{-1}. The existence of an aromatic component in the polymer films is desirable for etch resistance in subsequent patterning steps. Beyond the expected peak broadening associated with the amorphous nature of the PECVD film, the plasma-deposited polymer has a carbonyl peak at around 1700 cm^{-1} not found in PHOST.

Among the many variables in plasma synthesis, we have found that the deposition pressure, RF power, and oxygen to hydrocarbon flow ratio have the most dramatic effect on deposition rate, glass transition temperature (T_g), and the ratio of O-H to C-H$_x$ in the films. In general, the deposition rate is most strongly affected by the pressure. All other parameters being constant, the deposition rate increases almost linearly from 150 to 650 nm/min as pressure is increased from 500 to 1500 mTorr. The T_g of these films, as deduced from the onset of softening in a TMA trace, is most strongly affected by the RF power. For example, films deposited at 1500 mTorr at powers of 100, 200, and 300 W had a T_g of 80, 90, and 105°C, respectively.

A key component of the plasma synthesis for this resist scheme is the formation of hydroxyl bonds in the polymer which, when exposed to a silicon-containing gas, react to incorporate silicon into the film. Figure 4-2 plots the deposition rate and the integrated FTIR O-H to C-H$_x$ ratio for films deposited from benzene and oxygen for varying oxygen flow rates. The pressure and power were fixed at 700 mTorr and

24

275

14

250

12

DEPOSITION RATE (nm/min)

225

10

[O-H] / [C-H$_x$] RATIO

200

8

175

6

4

150

2

0   25   50   75   100   125

O$_2$ FLOW RATE (sccm)
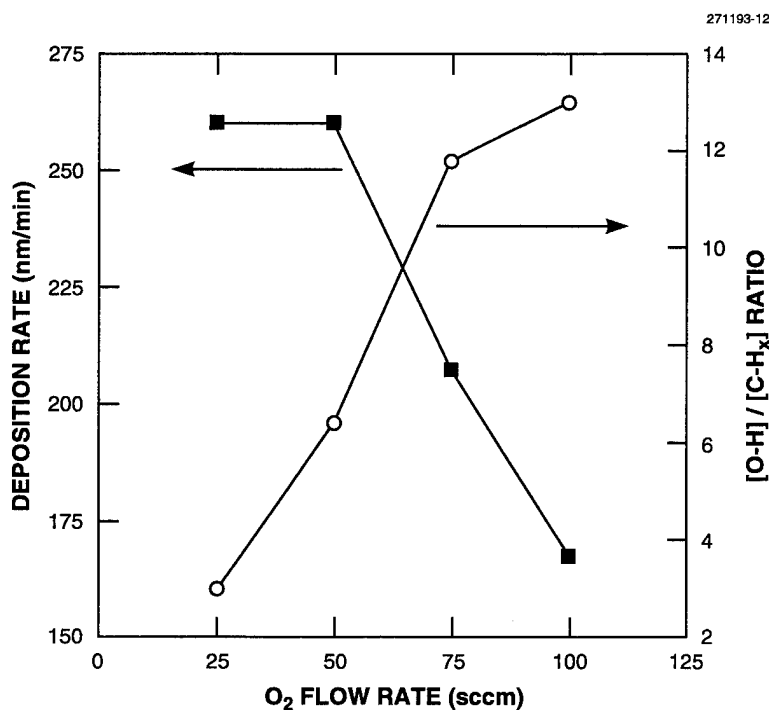
Figure 4-2. Deposition rate and integrated [O-H]/[C-H$_x$] ratio for films deposited from benzene at various flow rates of oxygen.

150 W, respectively. The benzene was introduced directly, i.e., without the use of a mass flow controller. As the oxygen flow rate increases, the deposition rate decreases while the O-H to C-H$_x$ ratio increases. We believe that the decrease in deposition rate with increased oxygen flow is a result of the competition between deposition and etching processes. The increase in O-H to C-H$_x$ ratio with increased oxygen flow rate is attributed to an increase in availability of oxygen.

The reactivity of the hydroxyl sites to a silylamine gas is shown in Figure 4-3. This figure plots the FTIR absorbance spectra of a film deposited from benzene and oxygen after exposure to DMSDMA at 55°C and 10 Torr for various times. As the silylation time increases, more silicon is incorporated, as indicated by the increase in the Si-H stretch peak at 2185 cm^{-1} and in the C-H$_3$ asymmetric stretch peak at 2950 cm^{-1}, both of which are associated with a dimethylsilyl group. There is also a corresponding decrease in the O-H peak and an increase in the Si-O-C (located at 923 cm^{-1} but not shown) with longer silylation time, indicative of the reaction between the silicon-containing gas and the hydroxyl groups [3]. The silylation process for these films is linear as seen both with FTIR and scanning electron microscopy cross-sectional staining, indicating that the rate-limiting step is not Fickian diffusion. The absolute silylation rate is a strong function of temperature; the films exhibit activation energies for diffusion from 0.55 eV, which is similar to that reported for DMSDMA in PHOST [4], to > 1.0 eV, depending upon deposition conditions.
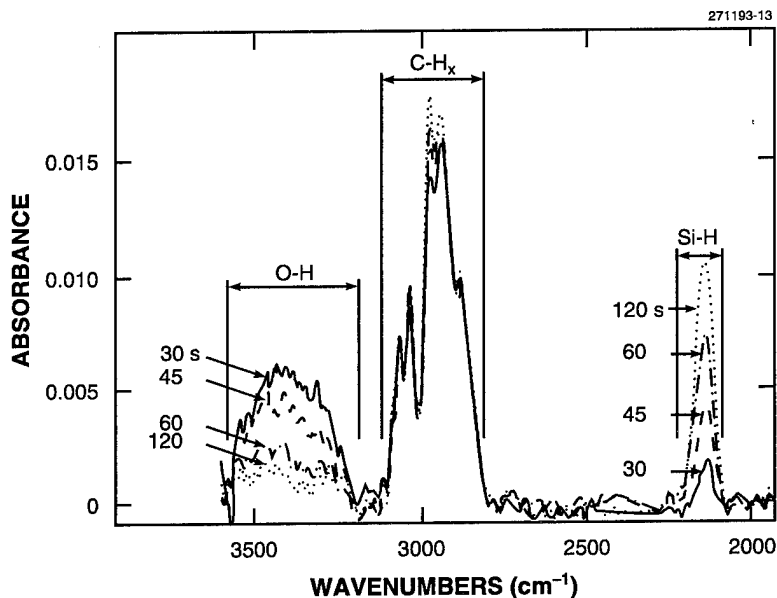
Figure 4-3. Time sequence of FTIR absorbance spectra of a film deposited from benzene and oxygen silylated with dimethylsilyldimethylamine (DMSDMA) at 45°C and 10 Torr for silylation times of 30, 45, 60, and 120 s.

The photosensitivity of these PECVD films is a direct measure of how effective the material is, when crosslinked by 6.4-eV photons, in retarding the diffusion of a gaseous silylating agent. For many spin-applied phenolic resists, 193-nm radiation is strongly absorbed causing homolytic, free-radical crosslinking of the resist [4]. The presence of a cyclic/aromatic component in these PECVD films (see Figure 4-1) is believed to be important in facilitating the crosslinking step, thereby controlling photosensitivity. We have used the sequence of open frame exposure, silylation to a fixed depth, and pattern transfer with 10% overetch to assess relative photospeeds of these resists. We have seen photospeeds from 30 to 300 mJ/cm^2 for polymers deposited from different precursors and under different plasma conditions, compared to 45 mJ/cm^2 for PHOST silylated to a thickness of 200 nm.

The lithographic contrast of the silylation process is evaluated by inferring the silicon uptake from the integrated Si-H peak as a function of dose. As in PHOST, the silylation contrast is rather low, ~ 1, but the contrast after pattern transfer is much higher, approaching 20. The optical density (OD) at 193 nm is also important to the lithographic performance of this resist, because it determines the photocrosslinking depth. For spin-applied 193-nm silylation resists, the crosslinked layer is typically < 70 nm thick, while the depth of silicon incorporation necessary for pattern transfer is much greater. This relatively thin crosslinked layer does not prevent isotropic diffusion under it, thus potentially compromising the ultimate lithographic performance for sub-0.25-μm lithography. The OD for films formed from benzene and oxygen is 2-4 μm^{-1}, much less than that of PHOST (25 μm^{-1}) and corresponding to the depth necessary to prevent isotropic diffusion. Selective silylation, and thus the lithographic capability, of PECVD silylation photoresist is demonstrated in Figure 4-4, which shows an example of residue-free

26

271193-14

1 μm
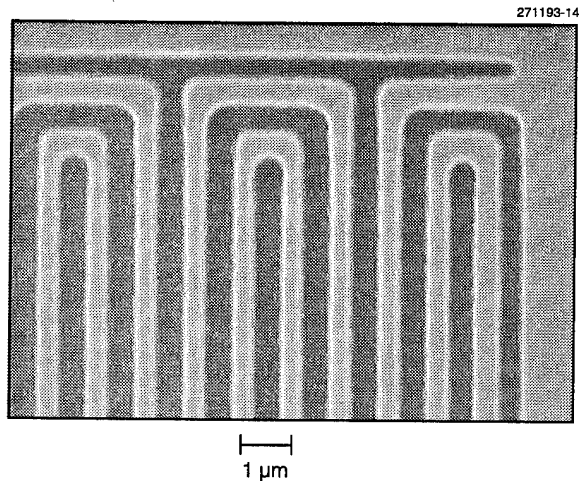
Figure 4-4. Scanning electron micrograph of 0.4-μm features printed with the positive-tone all-dry silylation resist deposited from cycloheptatriene and oxygen. Exposure was done on a modified 193-nm GCA 10× stepper at a dose of 135 mJ/cm². Silylation was performed using DMSDMA at 85°C and 10 Torr for 90 s. Pattern transfer was performed in a helicon etcher using oxygen for 80 s yielding 200% overetch.

0.4-μm features patterned in a 0.70-μm-thick film deposited from cycloheptatriene and oxygen. The sample was exposed to a dose of 135 mJ/cm², silylated at 85°C and 10 Torr with DMSDMA for 90 s, and pattern transferred for 80 s in a helicon reactor yielding 200% overetch (oxygen plasma). These are initial results of this novel process. We expect that significantly higher resolution can be obtained as the process is further refined, and with the use of higher-numerical-aperture projection optics.

M. W. Horn   R. B. Goodman
M. Rothschild   R. R. Kunz
B. E. Maxwell   L. M. Eriksen

4.2   FIELD EMISSION FROM NITROGEN-DOPED DIAMOND

Diamond has a negative electron affinity (NEA) [5]–[8], that is, the minimum energy of electrons in the conduction band is above the minimum energy of electrons in vacuum. This has made possible the realization of electron diode emitters [9],[10], and has motivated others to characterize electric field emission from diamond [11]–[14]. However, to take advantage of diamond's NEA property, a source of electrons must be present either in the conduction band or in a sub-band near the vacuum energy level [14].

Nitrogen forms a deep electron donor ~ 1.7 eV below diamond's conduction band [15], and we have observed electron emission from nitrogen-doped diamond at vacuum electric fields of 0–1–V μm^{-1}. However, because these diamonds are very resistive, a substantial voltage, several thousand volts, is dropped in the 1- to 2-mm-thick diamond substrate. These results should be contrasted to the behavior of polycrystalline boron-doped (p-type) diamond. This material is highly conductive and does not exhibit a significant voltage drop across the substrate, but it requires high fields, 20–50 V μm^{-1}, to obtain emission.

Type Ib diamond substrates, doped to ~ 10^{19} cm^{-3} with nitrogen, were obtained from commercial sources for use in this study. One set of experiments used (100)-oriented, cut and polished diamonds. The other experiments used wire-drawing dies (synthetic high-pressure diamonds used as dies for wire drawing) that consisted of cubo-octahedrons, faceted on (111) and (100) crystal planes, 2–3 mm on a side. All these substrates were cleaned [14] prior to mounting in a 10^{-6} Pa ion- or a cryo-pumped vacuum system.

Electrical contact to the boron-doped diamond can be made with a clip, but type Ib substrates are insulating and the back-metal contact was found to be the limiting factor for both conduction through and emission from the diamond. Contact to the diamond was made by enhancing field emission of electrons into the diamond with a rough metal-diamond interface. Two techniques were employed to obtain this interface. One used either Ni or Ni salts on the back of the diamond, annealed in a mixture of Ar and H_2 at 900–1080°C for several minutes. The Ni or the Ni metal formed from the metal salts during annealing etches pits in the substrate by catalyzing a reaction between diamond and H_2 to form CH_4. The other technique used anisotropic dry etching [16] to roughen the diamond surface, which was later covered with vacuum-evaporated Ni to make electrical contact. Both techniques increased the conductivity though the diamond. Figure 4-5(a) compares the conductivity through 1 mm of type 1b diamond for a smooth and rough interface. Conduction through these diamonds usually approximates a straight line when plotted in Fowler-Nordheim [17] coordinates (current through the diamond divided by the voltage across the diamond squared plotted against the inverse of the voltage), as shown by Figure 4-5(b).

Field emission measurements were made by placing a 1-mm-diam Mo anode at various heights above the sample. As seen in Figure 4-6, the emission is nearly independent of substrate-anode spacing from touching to 400 μm, and only decreases when this spacing is larger than the lateral dimensions of the diamond substrate, ~ 5 mm. An estimate of the field between the substrate and the anode can be obtained by plotting the voltage required to obtain a given emission current for several substrate-anode spacings. The slope of the straight line fit to the data is the average vacuum field, and the intercept at zero spacing is the internal potential across the substrate. Figure 4-7 compares data from nitrogen-doped diamond and boron-doped diamond when plotted in this manner. Conductive boron-doped diamond does not support a measurable potential across the substrate, but requires a substantial field to obtain emission. Type Ib diamond requires a vacuum field of only ~ 0.2 V μm^{-1}, but a potential of several kilovolts appears across the substrate.
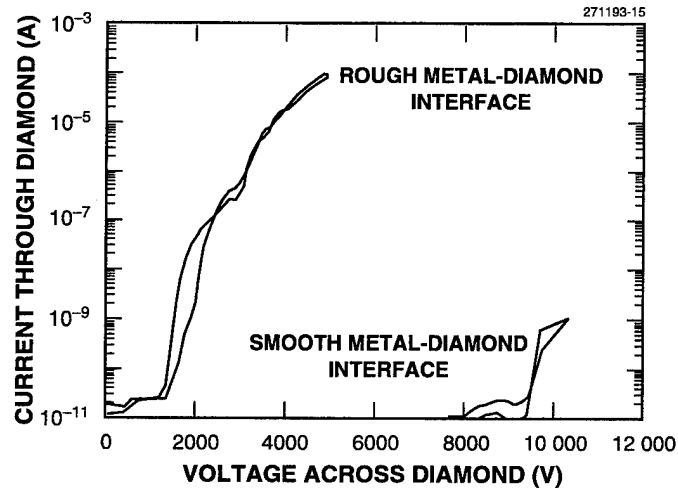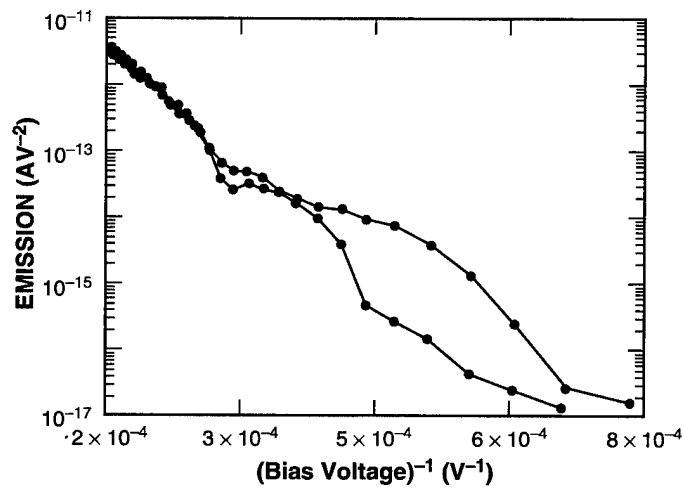
Figure 4-5. (a) Comparison of conductivity through two halves of the same 1-mm-thick, polished, type Ib diamond. The back contact consisted of a smooth interface with 100 nm of electron-beam-evaporated Ni and a roughened interface with a Ni salt deposited on the diamond and annealed in H_2 and Ar at 1080°C for 30 min (an additional 100 nm of Ni was evaporated on the back of the diamond to ensure electrical contact). (b) Results for the roughened interface plotted in Fowler-Nordheim coordinates.
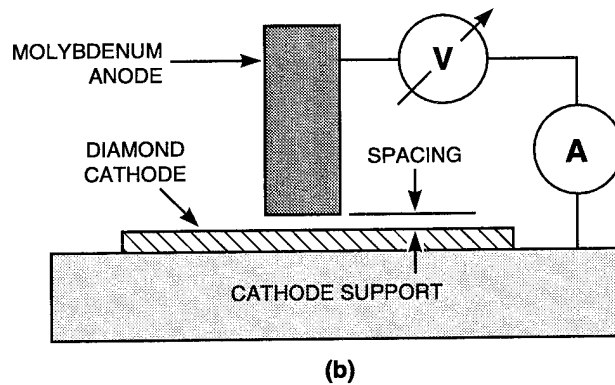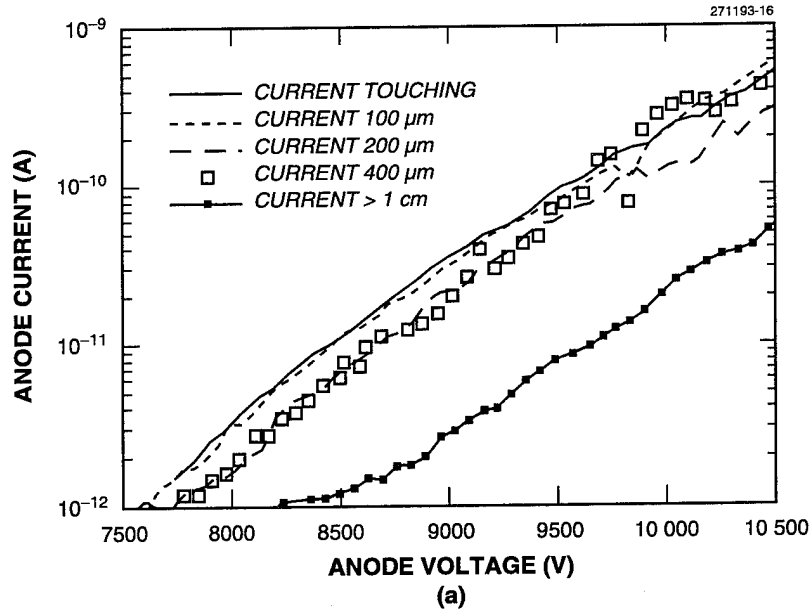
Figure 4-6. Emitted current as a function of anode voltage for several substrate-anode spacings. The back contact was roughened as described in the caption of Figure 4-5.
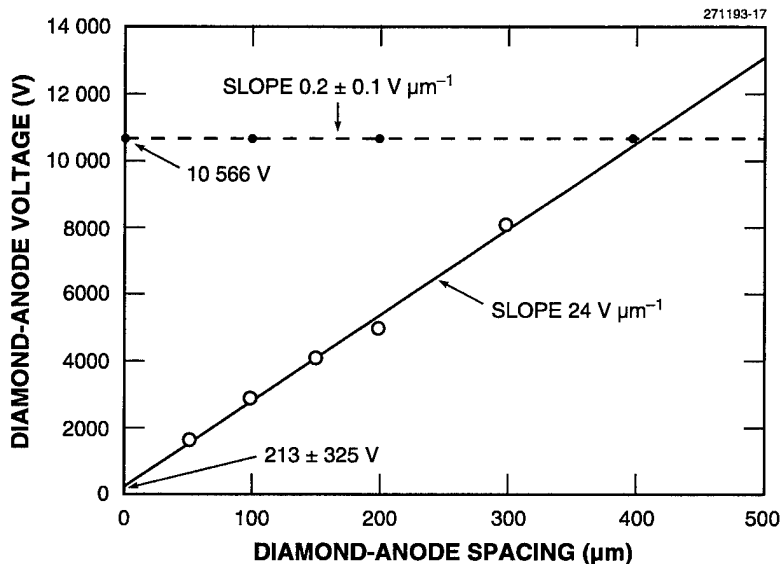
*Figure 4-7. Voltage required for field emission of 1 × 10⁻⁹ A cm⁻² for boron-doped diamond (open circles) and type Ib diamond (solid circles) as a function of substrate-anode spacing.*

The emission from both polished and as-grown wire-drawing type Ib diamonds appears the same. The electrons are either emitted as a diffuse unstructured beam or as many small beamlets. Diffuse beams are emitted from diamonds that have been coated with Cs, as described in [14], while the uncoated diamonds usually emit beamlets. These beamlets are emitted at angles up to 45° from the substrate normal. By using a movable phosphor screen it was determined that small regions < 100 μm in diameter were responsible for several beamlets emerging at angles several tens of degrees from each other. When the emitted current is > 0.1 mA, glowing channels often appear in the diamond that extend from the back contact to the top of the diamond. The source of beamlets appears to correspond to the top of these glowing channels. Often the beamlets would be so energetic that they would miss the anode ~ 100 μm from the diamond surface and strike the anode's metal fixturing several millimeters away. When the emitted current is ~ 0.1–1 mA, the electrons emitted from the diamond have sufficient energy to cause the anode to glow red hot. This is known to require power levels ≥ 1 W, which necessitates that the average electron energy be several kilovolts. This electron energy is considerably larger than the ~ 100 eV that the electrons could obtain traveling from the diamond surface to the anode when the vacuum field is ≤ 1 V μm⁻¹.

The emission characteristics of the boron-doped and nitrogen-doped diamond can be explained as follows. Boron-doped diamond has effectively no conduction band electrons and a work function of 4.8–7.8 eV [7], requiring electric fields of 20–50 V μm⁻¹ to obtain electron emission from rough poly-crystalline surfaces, the same field necessary for field emission from high-work-function metals, like W or Mo. For nitrogen-doped diamond, where the substrate is insulating at low fields, < 0.1 V μm⁻¹, the

31

emission is dependent upon the back interface. The nitrogen dopant forms a depletion region at the back metal-diamond interface which allows for tunneling of electrons into the diamond. A rough surface at the interface enhances the electric field locally and facilitates electron tunneling. Once in the diamond, electrons travel through the diamond under the influence of an internal electric field and are emitted from the diamond surface. The NEA property allows the emission of electrons into the vacuum with minimal vacuum field. Some of the emitted electrons appear to leave the diamond surface with considerable energy, > 1 keV. We are uncertain where the electrons are accelerated. This energy could be due to high fields just above or just below the diamond surface or to electron channeling through the diamond. The diamonds often glow during emission, and this may indicate the presence of conduction channels [18] which can form in semiconductors under high internal fields. Where these several kilovolt electrons are accelerated is being investigated. Several groups have reported electrons being accelerated to high energies, 5–60 eV, in insulators [19] and semiconductors [20]. Cuttler [21] has predicted higher electron energies, ~ 1 keV, in diamond when subjected to fields > 100 V μm^{-1}.

M. W. Geis   K. Krohn

J. C. Twichell   T. M. Lyszczarz

N. N. Efremow

REFERENCES

1. M. W. Horn, S. W. Pang, and M. Rothschild, *J. Vac. Sci. Technol. B* **8**, 1493 (1990).

2. A. T. Wiedman and A. M. Joshi, *Appl. Phys. Lett.* **62**, 372 (1993).

3. M. A. Hartney, M. Rothschild, R. R. Kunz, D. J. Ehrlich, and D. C. Shaver, *J. Vac. Sci. Technol. B* **8**, 1476 (1990).

4. D. W. Johnson and M. A. Hartney, *Jpn. J. Appl. Phys.* **31**, 4321 (1992).

5. F. J. Himpsel, J. A. Knapp, J. A. Van Vechten, and D. E. Eastman, *Phys. Rev. B* **20**, 625 (1979).

6. B. B. Pate, B. J. Waclawaski, P. H. Stefan, C. Binns, T. Ohte, M. H. Hecht, P. J. Jupter, M. L. Shek, D. T. Pierce, N. Swanson, R. J. Celotta, I. Liundau, and W. E. Spicer, *Physica B* **117/118**, 783 (1983).

7. M. W. Geis, J. A. Gregory, and B. B. Pate, *IEEE Trans. Electron Devices* **38**, 619 (1991).

8. J. van der Weider and R. J. Nemanich, *Phys. Rev. B* **45**, 13629 (1994).

9. M. W. Geis, N. N. Efremow, J. D. Woodhouse, M. D. McAleese, M. Marchywka, D. C. Socker, and J. F. Hochedez, *IEEE Electron Device Lett.* **12**, 456 (1991).

10. G. R. Brandes, C. P. Beetz, C. A. Feger, and R. L. Wright, *Diamond Related Mater.* **4**, 586 (1995).

11. M. E. Kordesch, *Proceedings of the 3rd International Symposium on Diamond and Diamondlike Materials*, J. P. Dismukes and R. K. Ravi, eds. (Electrochemical Society, Pennington, N.J., 1993), p. 787.

12. J. C. Twichell, M. W. Geis, C. O. Bozler, D. D. Rathman, N. N. Efremow, K. E. Krohn, M. A. Hollis, R. Uttaro, T. M. Lyszczarz, M. E. Kordesch, and K. Okano, presented at *Diamond Films '93*, Albufeira, Portugal, 20–24 September 1993.

13. K. Okano, K. Hoshina, and M. Iida, *Appl. Phys. Lett.* **64**, 2742 (1994).

14. M. W. Geis, J. C. Twichell, J. Macaulay, and K. Okano, *Appl. Phys. Lett.* **67**, 1328 (1995).

15. H. B. Dyer and L. du Preez, *J. Chem. Phys.* **42**, 1898 (1965).

16. N. N. Efremow, M. W. Geis, D. C. Flanders, G. A. Lincoln, and N. P. Economou, *J. Vac. Sci. Technol. B* **3**, 416 (1985).

17. A. van der Ziel, *Solid State Physical Electronics* (Prentice-Hall, N.J., 1966), pp. 144–146.

18. M. A. Lampert and P. Mark, *Current Injection in Solids* (Academic, N.Y., 1970), p. 276.

19. H. J. Fitting and A. von Czarnowski, *Phys. Status Solidi A* **93**, 385 (1986).

20. G. O. Muller, R. Mach, G. U. Reinsperger, E. Halden, and G. Schulz, *J. Cryst. Growth* **117**, 948 (1992).

21. P. Cuttler, private communication.

5. HIGH SPEED ELECTRONICS

5.1 SELF-ALIGNED COMPLEMENTARY GaAs MISFET USING A LOW-TEMPERATURE-GROWN GaAs GATE INSULATOR

A self-aligned n-channel metal-insulator-semiconductor FET (MISFET) with very low gate leakage current has been developed using a low-temperature-grown (LTG) GaAs gate insulator [1]. The MISFET is ideal for digital circuits because it provides high noise margin and low static power consumption. Recently developed self-aligned p- and n-channel MISFETs fabricated on the same wafer are reported here to demonstrate the feasibility of using LTG-GaAs MISFETs for complementary logic circuits.

The epitaxial layers were grown by molecular beam epitaxy on a semi-insulating GaAs substrate, as shown in Figure 5-1(a). The layers consist of a 3000-Å-thick GaAs channel, a 100-Å-thick AlAs barrier, a 300-Å-thick LTG-GaAs gate insulator, a 100-Å-thick AlAs barrier, and a 100-Å-thick GaAs cap. None of the layers was intentionally doped, but the undoped GaAs channel was slightly p-type with a background hole concentration of $\sim 10^{15}$ cm^{-3}. The growth temperature was 600°C for all the layers except for the LTG GaAs, which was grown at 200°C and then annealed at 600°C for 10 min before growing the AlAs barrier and GaAs cap on top. The 3-in. wafer with these epitaxial layers was then cleaved into several pieces for the fabrication of normally-off p-channel and both normally-off and normally-on n-channel MISFETs. Each piece had only one type of MISFET on it and the same mask set was used for all devices.

A simplified illustration of the fabrication sequence is shown in Figure 5-1(b). For the normally-on n-channel MISFET, the doped n-channel was first formed by Si implantation without a mask. The implant energy and dose were 115 keV and 7×10^{12} cm^{-2}, respectively. Then the gate metal, consisting of 700 Å of W and 2000 Å of Au, was deposited by evaporation and patterned by optical lithography and liftoff on all three pieces. Next, the source and the drain regions were implanted using the W/Au gate metallization as a self-aligned mask. For the two n-channel pieces, Si was used to form the n^+ regions with an implant energy of 60 keV and a dose of 3.0×10^{13} cm^{-2}. For the p-channel piece, Be was used to form the p^+ regions with an implant energy of 24 keV and a dose of 4.7×10^{13} cm^{-2}. After the implantation, the Au metal was etched off and the wafers were annealed at 825°C for 10 s using a GaAs substrate as the proximity anneal cap. Next, the source and drain ohmic regions were defined in photoresist and the gate insulator layers were wet etched in the exposed ohmic regions to the top of the GaAs channel. Then the ohmic-contact metal was evaporated and defined by liftoff using the same photoresist that was patterned for the etching, and this was followed by alloying. The ohmic metallizations were Ni/Ge/Au for the n-channel and Au/Zn/Au for the p-channel MISFETs. Finally, devices were isolated by proton implantation. The gate length and width of the MISFET were 1.5 and 100 μm, respectively, and the spacing between the source and drain ohmic contacts was 7 μm.

The drain current vs voltage (I_{ds}-V_{ds}) characteristics of MISFETs are shown in Figure 5-2. As expected, the maximum I_{ds} of the normally-off n-channel MISFET is small (40 mA/mm at the gate voltage V_{gs} = +4.5 V), and the device has a very high output resistance. As shown in Figure 5-2(b), the threshold voltage is 1.3 V. For the normally-on n-channel MISFET, the maximum I_{ds} is $\sim$ 500 mA/mm

because of the Si implant in the channel. As shown in Figure 5-2(a), a V_{gs} of –2.4 V is required to pinch off the device. Figure 5-2(c) shows that I_{ds} for the p-channel MISFET reaches a maximum of 120 mA/mm at $V_{gs} = -8$ V. The maximum g_m of 22 mS/mm measured at $V_{gs} = -5$ V is comparable to that of the best GaAs/AlGaAs p-channel heterojunction FET having a similar gate length. The important device parameters are summarized in Table 5-1.
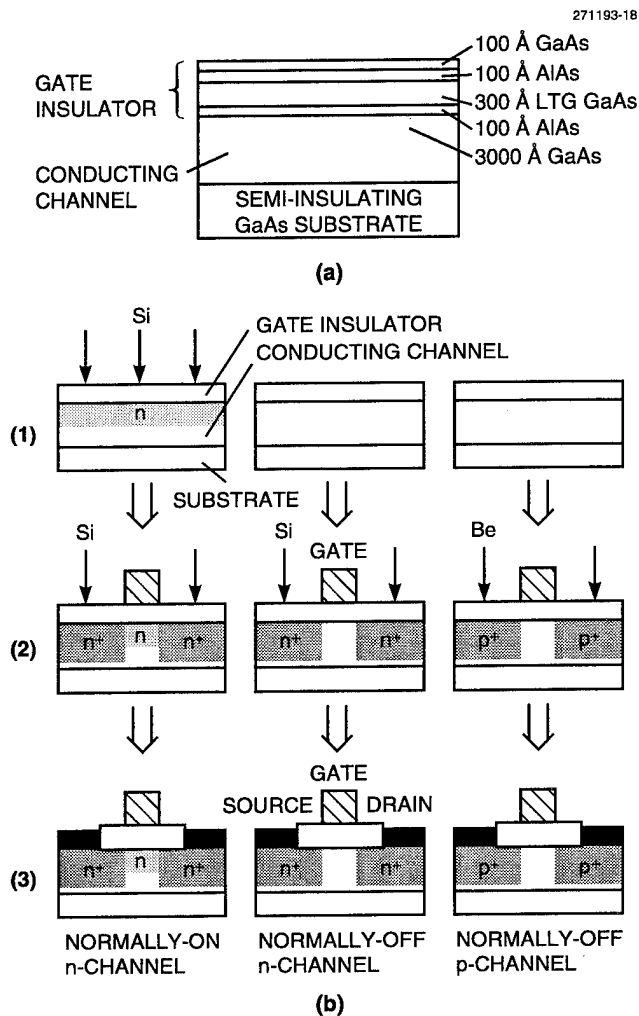

Figure 5-1. (a) Layer structure and (b) fabrication sequence for p- and n-channel low-temperature-grown (LTG) GaAs metal-insulator-semiconductor FETs (MISFETs).

36
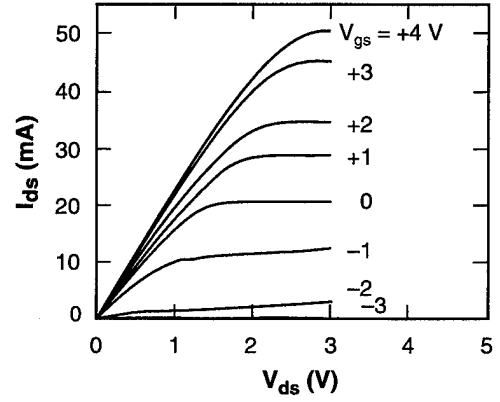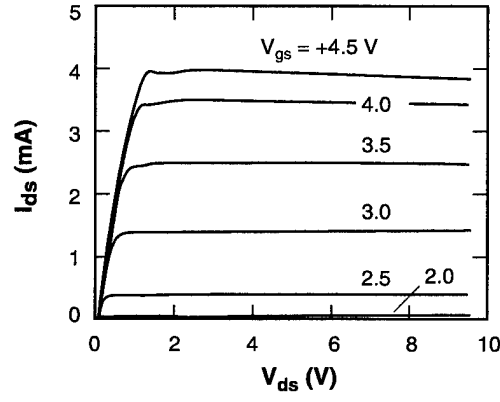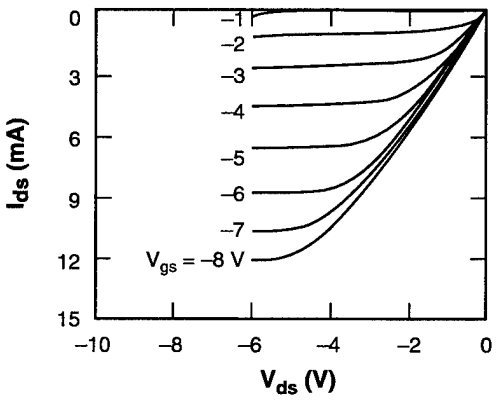
Figure 5-2. I_{ds}-V_{ds} characteristics of 100-μm-wide LTG-GaAs MISFETs: (a) normally-on n-channel, (b) normally-off n-channel, and (c) normally-off p-channel.

TABLE 5-1

Device Parameters for Metal-Insulator-Semiconductor FETs

	n-Channel Normally-On	*n*-Channel Normally-Off	*p*-Channel Normally-Off
Maximum I_{ds} (mA/mm)	500	40	120
V_{gs} for maximum I_{ds} (V)	+4.0	+4.5	−8.0
Maximum g_m (mS/mm)	114	25	22
Threshold voltage V_t (V)	−2.4	+1.3	−1.2
Reverse gate breakdown (V)	−10	−40	+7

The amount of the forward-biased gate current of all three MISFETs is very similar and the I_{gs}-V_{gs} relationship follows the typical trap-limited current patterns, indicating that the conduction is determined mainly by the LTG-GaAs layer. At 1 V of forward bias, the gate current is ~ 0.1 μA/mm gate width, which is equivalent to 6.6×10^{-10} A/μm^2 gate area. By using the conventional definition of I_{gs} at 1 mA/mm, the gate forward turn-on voltage is close to 3 V, which is much higher than the 0.7 V for a MESFET. Since the forward-biased gate current is very sensitive to the quality of the LTG insulator, our results indicate that implanting Si through the LTG-GaAs gate insulator of the normally-on *n*-channel MISFET did not degrade the resistivity of the LTG GaAs.

The significance of this work is the demonstration of a new family of MISFETs ideal for complementary logic circuits, even though the device parameters are not optimized. The results reported here show that the LTG-GaAs MISFET can sustain the ion implantation for both channel and source-drain doping without noticeable degradation. In addition, the threshold voltage and the drain current of MISFETs on the same wafer can be easily adjusted by the channel implant. Other than replacing a GaAs substrate with an epitaxial wafer, all the processes for complementary LTG-GaAs MISFETs are industry standards for self-aligned GaAs MESFET integrated circuits.

C. L. Chen   L. J. Mahoney
K. B. Nichols   E. R. Brown

REFERENCE

1.   C. L. Chen, L. J. Mahoney, K. B. Nichols, M. J. Manfra, B. F. Gramstorff, K. M. Molvar, R. A. Murphy, and E. R. Brown, *IEEE Electron Device Lett.* **16**, 199 (1995).

6. MICROELECTRONICS

6.1 NOISE ANALYSIS OF AN ELECTRONICALLY SHUTTERED AND BACK-ILLUMINATED CCD PIXEL

Noise measurements are reported for an electronically shuttered, back-illuminated pixel [1] structure under high photon flux (shot noise limited) conditions. Measurements show that over a certain operating range, the electronic shutter suppresses the input shot noise more than the corresponding average signal of the photogenerated electrons, resulting in an improvement in the overall signal-to-noise ratio. The electronic shutter causes noise suppression by correlating the collected photoelectrons that are generated by an incoming light signal over an integration period. The shutter creates a nonlinear signal-dependent collection efficiency similar to the avalanche photodiode analyzed in [2]. During an integration period, this nonlinear collection efficiency causes an anticorrelation between the photoelectrons already accumulated in the pixel well and the photoelectrons still to be collected.

Figure 6-1 shows impurity and potential profiles vs depth below the surface of the collection well where the potential profiles are given for two different bias conditions. A detailed description of the electronic shutter fabrication and operation are given in [1]. The bias conditions in Figure 6-1(c) cause the depletion region to extend deep into the high-resistivity (> 3000 Ω cm) p-type substrate. Photoelectrons created in the substrate are accelerated by the electric field to the pixel well as in a conventional back-illuminated charge-coupled-device (CCD) pixel. For a constant photon flux, the collected electron signal varies linearly with time. In Figure 6-1(b), the voltage bias on the imaging array gate electrode causes the depletion edge to terminate in the relatively high doped ($\sim 3 \times 10^{16}$cm^{-3}) p barrier region. The undepleted portion of the p barrier region creates a potential barrier that reduces the number of photoelectrons, generated in the low-doped p substrate, that reach the pixel collection well. As more electrons are collected in the well, the depletion region continues to collapse and the barrier height increases. The increasing barrier height with collected electron signal gives a nonlinear signal-dependent collection efficiency. As the well continues to fill, the barrier height eventually becomes constant to the photoelectrons generated in the bulk.

Figure 6-2(a) shows the standard deviation vs average signal on a logarithmic scale, and Figure 6-2(b) is a plot of the variance vs average signal on a linear scale. Each point displayed represents one pixel in a 16 × 64 section of the 64 × 64-pixel imaging array. The result for a particular pixel is an average calculated from 400 image frames. The varying pixel signals are created by a spatially nonuniform light source illuminating the array. At low signal levels, the slope of the log curve in Figure 6-2(a) is 1/2, as would be expected for linear collection of a Poisson-distributed photoelectron signal. However, as the signal increases, the slope falls below 1/2, indicating noise suppression at the higher signal levels. Also shown in Figure 6-2(a) is the pixel response that occurs when a gate voltage is applied that causes the depletion region to extend deep into the substrate. In this case, the collection of the photoelectron signal remains linear with time, as in an unshuttered pixel, and the slope of the curve has a value of 1/2 even at the highest signal shown. Figure 6-2(b) shows the same tendency as in Figure 6-2(a), where for a conventional shot-noise-limited signal the curve is linear, but for the shuttered pixel the curve is substantially sublinear. In fact, the variance is almost a factor of 2 lower than that of the shot-noise-limited input signal.

271193-20
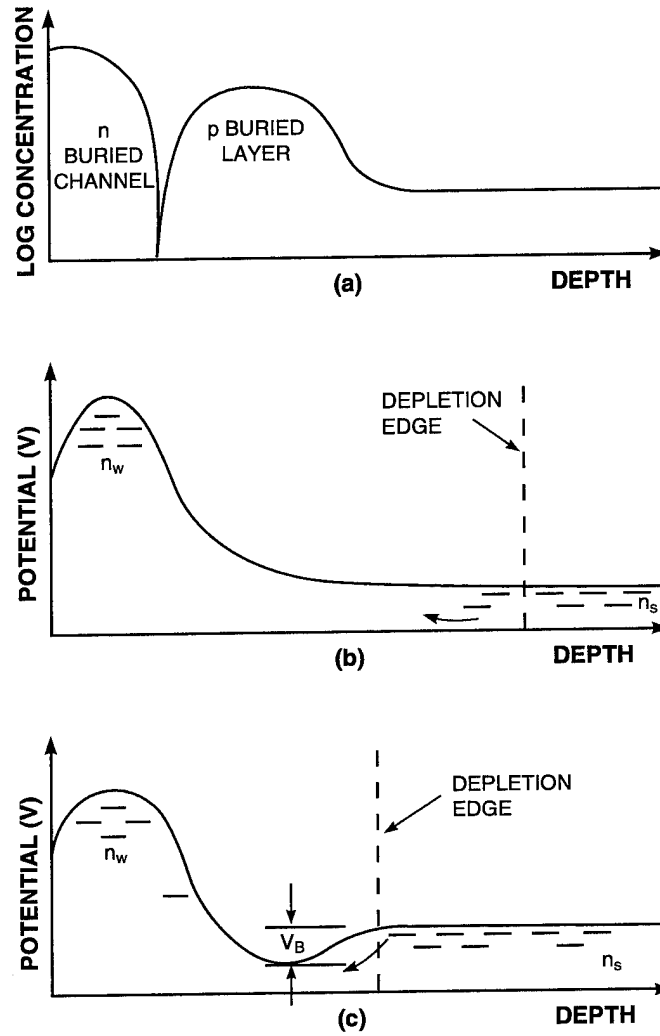
Figure 6-1. *(a) Doping profile vs depth for the shuttered pixel collection well; (b),(c) potential profiles for depletion region extending deep into substrate and for depletion region terminating in highly doped p barrier region, respectively.*

271193-21
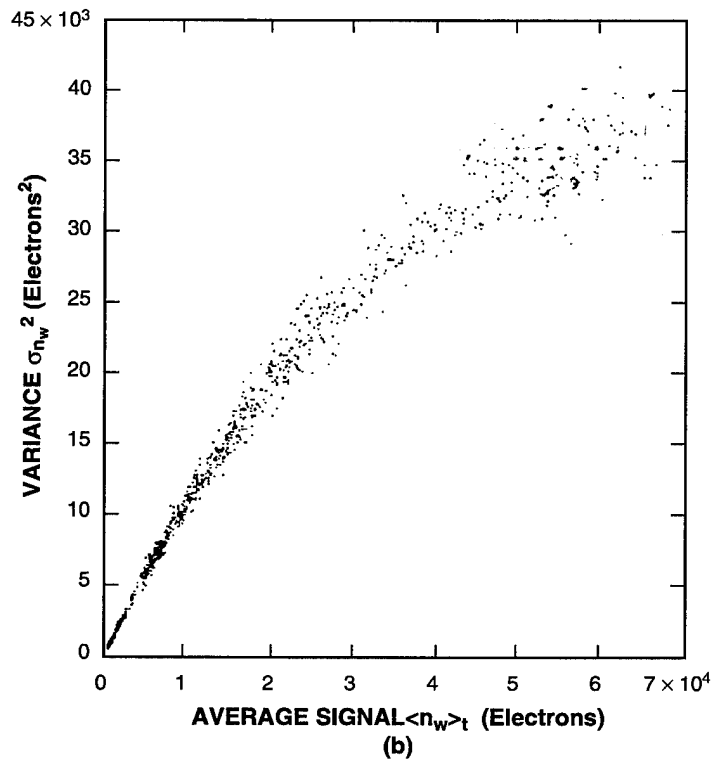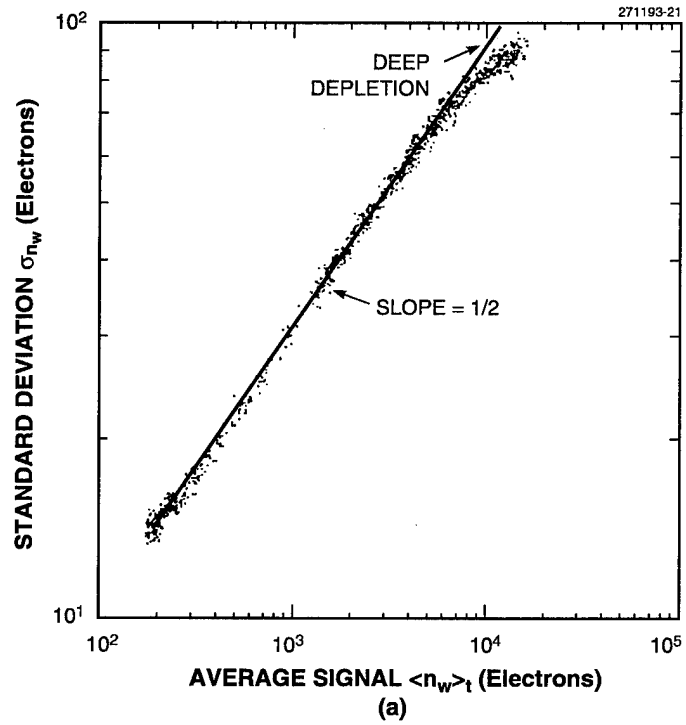
Figure 6-2. (a) Standard deviation σn_w vs average number of photoelectrons $<n_w>_t$ collected, shown on a logarithmic scale; (b) same data only now plotted as variance $\sigma n_w{}^2$ vs average signal on a linear scale.

41

The measurements indicate that the spread in the measured photoelectron distribution, created by a shot-noise-limited and constant flux light signal, is less than that corresponding to a Poisson distribution. For the highest signal level given in Figure 6-2, the squared output signal-to-noise ratio is increased by a factor of 1.75 over that of the shot-noise-limited input.

R. K. Reich

REFERENCES

1. R. K. Reich, R. W. Mountain, W. H. McGonagle, C. M. Huang, J. C. Twichell, B. B. Kosicki, and E. D. Savoye, *IEEE Trans. Electron Devices* **40**, 7 (1993).

2. Z. S. Huang, *IEEE Trans. Electron Devices* **41**, 9 (1994).

7. ANALOG DEVICE TECHNOLOGY

7.1 MICROWAVE INTERMODULATION PRODUCTS IN $YBa_2Cu_3O_{7-x}$ JOSEPHSON JUNCTIONS AND THE COUPLED-GRAIN MODEL

The generation of intermodulation products (IMPs) by microwave components is undesirable in almost all applications. Normal metals and most dielectrics have linear electrical properties up to very high fields and currents, and therefore passive microwave components made from them produce very little intermodulation distortion. On the other hand, components made from the high-transition-tempera-ture superconductors have shown relatively higher nonlinearities, which lead to power-dependent losses and higher levels of IMPs [1]. It is believed that the dominant mechanism for these nonlinearities is Josephson-junction-like weak links between grains of otherwise nearly ideal superconductor [2]. This coupled-grain model has been used to explain power-dependent losses in superconducting microwave resonators [3]. The purpose of this report is to present a first step toward determining whether the same coupled-grain model can also explain the observed IMP generation.

The coupled-grain model assumes that all the grains are of equal size and that all the Josephson junctions between them are identical. In practice, a film almost certainly contains a distribution of grain sizes and junction properties, which makes interpretation of experimental data difficult. To avoid this problem we have tested our models on an intentionally produced single, although spatially extended, Josephson junction. These results can easily be extended to more complex coupled-grain models.

We will analyze a single half-wavelength resonator with a Josephson junction intentionally placed in the center at $z = 0$, as shown in Figure 7-1. The current density through the junction is not uniform, peaking strongly at the edges of the resonator [4], but each small region of the junction can be considered as a resistively shunted Josephson junction (RSJ) with uniform current.
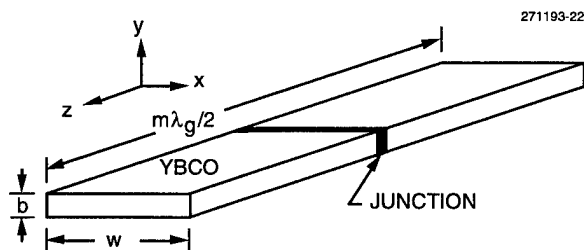

Figure 7-1. Microwave resonator with Josephson junction.

Currents applied simultaneously through a Josephson junction at two frequencies f_1 and f_2 will produce currents and voltages at many orders of sum and difference frequencies because of the junction nonlinearities, but the strongest IMPs near f_1 and f_2 will be the third-order ones (IM3s), at frequencies $2f_1-f_2$ and $2f_2-f_1$. We have calculated the IM3 voltage produced across an RSJ by numerically solving the usual RSJ circuit equations [5] in the time domain. Figure 7-2 shows the normalized third-order intermodulation voltage appearing across the junction vs the normalized current amplitude. The third-order intermodulation voltage V_3 is normalized by $I_C R$, where I_C is the junction critical current and R is the junction shunt resistance. The sum of the two equal applied current amplitudes $I_1 + I_2 = 2I$ is normalized by I_C. The different curves correspond to different values of the reduced frequency Ω, given by

$$\Omega = \frac{\omega}{2eI_C R/\hbar} ,$$ (7.1)

where $\omega = \pi(f_1 + f_2)$ is the average angular frequency, e is the electronic charge, and $\hbar$ is Planck's constant divided by 2π.

Figure 7-2 has several interesting features. At low applied current V_3 increases as $(2I/I_C)^3$, as would be expected from a third-order process. The amplitude of V_3 in this cubic region is well approximated by the expression

$$\frac{V_3}{I_C R} = \frac{0.02\Omega}{1+2.67\Omega^2+\Omega^4}\left(\frac{2I}{I_C}\right)^3 , \qquad \left(\frac{2I}{I_C}\right) \le 1 .$$ (7.2a)
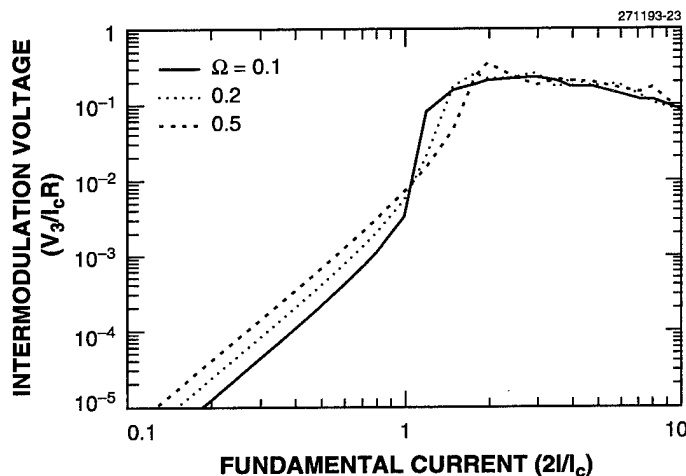

Figure 7-2. Third-order intermodulation voltage, normalized by $I_C R$, vs the current at each fundamental frequency.

As $2I/I_C$ exceeds 1 for lightly damped ($\Omega < 1$) junctions, V_3 increases more rapidly than cubic and then remains nearly constant. For $\Omega \ll 1$, as will be the case for junctions studied here, we will approximate this by a step change to

$$\frac{V_3}{I_C R} = 0.2 \ , \qquad \left(\frac{2I}{I_C}\right) > 1 \ . \tag{7.2b}$$

Figure 7-1 shows the center conductor of a stripline microwave resonator with a single Josephson junction across the center. The length of the resonator in the propagation direction is an integral number of half wavelengths, $m\lambda_g/2$, where λ_g is the wavelength at resonance on the transmission line from which the resonator is made, and the mode number m is a positive integer. The center conductor has width w in the x-direction and thickness b in the y-direction.

To find the resonator currents caused by voltages across the Josephson junction, we consider a half-wavelength-long resonator ($m = 1$) with a voltage source $V = V_1 \cos\omega t$ in the center, at $z = 0$, extending across the resonator but with negligible extent in the z-direction. This voltage produces a current in the resonator $dI(x) = dI_1(x) \cos\omega t$, where

$$dI_1(x) = bJ_1(x)dx = V_1 dY(x) \ . \tag{7.3}$$

Here $J_1(x)$ is the amplitude of the current density, assumed constant over the resonator thickness b. This expression defines the differential admittance

$$dY(x) = \frac{bJ_1(x)dx}{V_1} \ . \tag{7.4}$$

By reciprocity, the short-circuit current amplitude produced at $z = 0$ by a voltage source of amplitude V_3 at position x is

$$dI_3(x) = V_3(x)dY(x) \ , \tag{7.5}$$

so the total current amplitude from all voltage sources is

$$I_3 = \int_{-w/2}^{w/2} \frac{bJ_1(x)}{V_1} V_3(I,x)dx \ . \tag{7.6}$$

For our purposes V_3 is the IM3 voltage given by Equation (7.2), so its dependence on I has been included explicitly in Equation (7.6). Equation (7.6) is the expression that must be evaluated to calculate IM3 currents. They can then be compared to the currents at the applied frequencies. We will first derive an expression for $J_1(x)/V_1$, then generalize Equation (7.2) to yield $V_3(I,x)$.

We seek a relation between the resonator current and voltage amplitudes when the voltage appears at $z = 0$ between two halves of a resonator. This resonator is capacitively coupled at both ends to transmission lines of characteristic impedance Z_0. This admittance Y_1 can be calculated by standard techniques, bearing in mind that at resonance the length of each section of transmission line differs slightly from $l_g/4$ to account for the capacitive coupling to Z_0. The result at resonance is approximately

45

$$Y_1 = \frac{1}{2Z_0 \left[\alpha \lambda_g + (\omega C Z_0)^2\right]} ,$$ (7.7)

where C is the capacitance at each end of the resonator coupling it to external transmission lines terminated in their characteristic impedance Z_0, ω is the angular frequency, and α is the attenuation coefficient of the resonator transmission line. The characteristic impedance of the resonator is also Z_0. The derivation of Equation (7.7) has assumed $\alpha \lambda_g$, $\omega C Z_0 \ll 1$.

Van Duzer and Turner [6] give an approximate analytic form for the current density distribution of an isolated superconducting strip when $wb \gg \lambda^2$, which is in reasonable agreement with the more accurate numerical calculations of Sheen et al. [4] for stripline, so we will use the analytical expressions to calculate IMPs. It will be assumed that this field distribution is not changed significantly by the presence of the junction or the IMPs, and that the current is uniformly distributed through the film thickness. The former is approximately true for small relative levels of intermodulation power, and the latter will be approximately true for films less than 2λ thick, such as the films considered here.

The expressions of [6] yield the factor in Equation (7.6) that we seek:

$$\frac{J_1(x)}{V_1} = \frac{Y_1}{\pi b w} \left[1 - \left(\frac{2x}{w}\right)^2\right]^{-1/2} , \qquad x < \frac{w}{2} - \frac{\lambda^2}{2b}$$ (7.8a)

$$\frac{J_1(x)}{V_1} = \frac{1.165 Y_1}{\pi \lambda (wb)^{1/2}} \exp\left[-\left(\frac{w}{2} - |x|\right)\frac{b}{\lambda^2}\right] , \qquad \frac{w}{2} - \frac{\lambda^2}{2b} < x \le \frac{w}{2} ,$$ (7.8b)

where λ is the superconductor penetration depth.

Equations (7.2) are easily generalized to the situation in which the junctions are distributed along $z = 0$, as they are in the resonator in Figure 7-1. Since I and I_C flow through the same area, $2I/I_C$ can be replaced with $2J(I,x)/J_C$ in Equation (7.2).

The modified Equations (7.2) along with (7.8) supply all the information needed to evaluate Equation (7.6) for the IM3 current amplitude I_3 arising from the two fundamental signals, each with current amplitude I. The integrals over x, although somewhat unwieldy, can be solved in closed form.

Several resonator structures like that shown in Figure 7-1 were fabricated in $YBa_2Cu_3O_{7-x}$ (YBCO) from Josephson superconductor-normal-superconductor edge junctions made by Koren et al. [7]. Measurements of the loss arising from the junction in one particular structure were recently reported by Oates et al. [8]. They showed that the junction dominates the resonator nonlinear behavior until current densities exceed its J_C by an order of magnitude. We have made intermodulation measurements on the same junction as that measured by Oates et al., so a direct comparison can be made between our derived values and those in [8].

Figure 7-3 shows the calculated and experimental IM3 currents for this resonator at a temperature of 71 K. Power measurements were converted to currents in Figure 7-3 using expressions given in [9].

46

271193-24
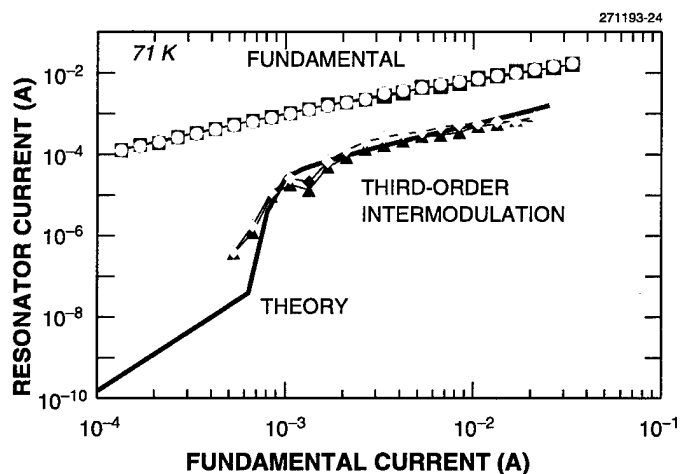
Figure 7-3. Fundamental and third-order intermodulation currents in stripline resonator at 71 K. The theoretical curve has no adjustable parameters.

We have used the values of R and J_C derived in [8] together with the calculations outlined above, so there are no adjustable parameters in the calculation of these IM3 currents. The agreement is excellent at this temperature, suggesting that the approximations made in the calculation are reasonable and that the RSJ model can give accurate results for YBCO Josephson junctions.

In future work we expect to compare the loss and intermodulation results for these Josephson junctions in resonators at different temperatures and external magnetic fields to further illuminate the physics of these YBCO junctions. In addition, we will determine whether the coupled-grain model can explain both the loss and intermodulation measurements from a YBCO film without intentional junctions.

T. C. L. G. Sollner
J. P. Sage
D. E. Oates

47

REFERENCES

1. N. Newman and W. G. Lyons, *J. Superconduct.* **6**, 119 (1993).

2. T. L. Hylton and M. R. Beasley, *Phys. Rev. B* **39**, 9042 (1989).

3. P. P. Nguyen, D. E. Oates, G. Dresselhaus, and M. S. Dresselhaus, *Phys. Rev. B* **48**, 6400 (1993).

4. D. M. Sheen, S. M. Ali, D. E. Oates, R. S. Withers, and J. A. Kong, *IEEE Trans. Microwave Theory Tech.* **39**, 1522 (1991).

5. F. Auracher and T. Van Duzer, *J. Appl. Phys.* **44**, 848 (1973).

6. T. Van Duzer and C. W. Turner, *Principles of Superconductive Devices and Circuits* (Elsevier, New York, 1981).

7. G. Koren, E. Polturak, D. Cohen, E. Aharoni, and L. Patlagan, *Physica C* **221**, 157 (1994).

8. D. E. Oates, P. P. Nguyen, Y. Habib, G. Dresselhaus, M. S. Dresselhaus, G. Koren, and E. Polturak, to be published in *Appl. Phys. Lett.*

9. D. E. Oates, A. C. Anderson, and P. M. Mankiewich, *J. Superconduct.* **3**, 251 (1990).

8. DIGITAL INTEGRATED CIRCUITS

8.1 ULTRAHIGH DENSITY PROM

A highly scaled programmable read-only memory (PROM) is being developed by taking advantage of ultimate lithographic resolution. This dense PROM device will be a nonvolatile, once-programmable, fast alternative to mass storage media such as compact disk read-only memory (CDROM), with zero standby power dissipation and no moving parts. The memory structure incorporates a vertically self-aligned diode and voltage programmable link (VPL) for a minimal memory cell area architecture just one lithographic line and space in each dimension. The densest arrays yet built, using conventional i-line lithography, have 0.6-μm lines and spaces, corresponding to a memory density of 70 Mbits/cm^2, while individual bits of 0.25-μm diameter have been built using phase-shift i-line exposure. The simple nature of the array makes phase shift lithography feasible, so with Lincoln Laboratory's unique 193-nm stepper, a memory array pitch of 0.2 μm is feasible, corresponding to the CDROM capacity of 640 Mbytes in 2 cm^2 of silicon. A transistor version of this device has been previously reported in [1],[2]. The diode form is a simpler, potentially denser version.

The basic memory element is a VPL and a diode in series. Operation of the single bit can be seen in Figure 8-1. This figure shows two traces, the first being before programming. For all biases less than +6 V, negligible current flows. Above 6-V forward bias, current starts to flow through the link insulator until at 10-V bias in Figure 8-1 the insulating dielectric breaks down, and a conducting filament forms resulting in a permanent electrical connection. The second trace shows the current after the link is formed, which is the characteristic of the diode, including reverse breakdown at –13 V in this case. A read cycle would occur at a word line bias of < 5 V, so the current difference between a programmed and unprogrammed bit is many orders of magnitude. The purpose of the diode, unnecessary for a single bit, is to provide isolation in a memory array.
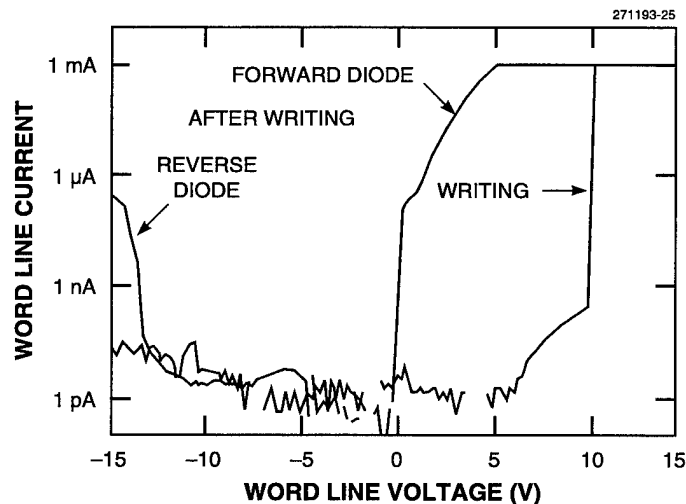

Figure 8-1. Conduction characteristics of a single bit, during and after writing. The first sweep shows picoamps for reverse bias and up to 6-V forward bias, with writing at +10 V. The second sweep shows diode reverse breakdown at –13 V and forward current limited at 1 mA.

In an array, illustrated in Figure 8-2, the read and write cycles are the same as a single bit with additional provisions for unselected lines. For the bit being accessed the word line is set high, forward biasing the diode, and the bit line is grounded. For all other bits, either zero or reverse bias is needed. All other bit lines are set high and all other word lines are grounded. In an $n \times n$ array, this results in one bit forward biased, $2(n-1)$ half-selected bits at zero bias, and the remaining nearly n^2 unselected bits reverse biased. The reverse leakage of a single diode is negligible, but the sum of all programmed, unselected bits could represent significant power dissipation during read. This current is minimized by small diode area, low sidewall leakage due to proper fabrication techniques, and read voltage much less than write voltage.

The starting material for fabricating this PROM is a two-layer epitaxial n-type growth on p-type silicon. The diode is formed in the top, lightly doped n-type layer, and the bottom, heavily doped n^+ region forms the bit line. The first step in PROM fabrication is to define the diode pillars (see Figure 8-2). The current process uses i-line lithography and reactive ion etching in He-Cl$_2$. The minimum feature size in arrays built thus far is 0.6 μm, and the etch depth is 1.0 μm. A second lithography step and 1.0-μm silicon etch define the n^+ bit lines. The severe topography generated by the two 1.0-μm silicon etches is then planarized using low-pressure chemical vapor deposition silicon dioxide from a tetraethylorthosilicate (TEOS) source followed by chemical-mechanical polishing (CMP) as described in [1]. The oxide layer is conformally deposited to fill the area between the pillars, and the wafer is then polished to remove the oxide from the pillar tops. This planarizing step results in a smooth surface with only the tops of silicon pillars exposed. An unmasked shallow p^+ implant forms the diode anode at the top of these exposed pillars. The VPL insulator trilayer, 5 nm each of silicon nitride, oxide, and nitride, is deposited by plasma-enhanced chemical vapor deposition, and contact holes are cut through the insulators to connect to the n^+ bit lines at the array periphery. Metal word lines and other interconnect are then sputter deposited and patterned.
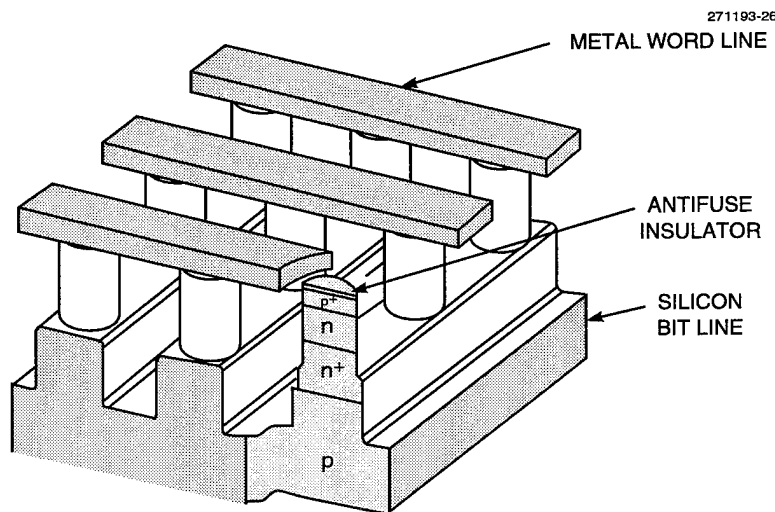

Figure 8-2. Schematic view of memory array. The space between silicon pillars is filled with silicon dioxide, which is planarized to provide a flat surface on which the link insulator and metal word lines lie.

Some of the critical steps include alignment of the two silicon etches, silicon pillar sidewall passivation, and CMP endpoint control. Misalignment during the bit line patterning leads to etching part of the previously defined pillar. A self-aligned process is being explored utilizing two crossed grating etches to define the pillars and bit lines. A second critical processing step is etch damage removal and passivation of the silicon sidewalls, especially in the region of the *pn* junction between the bit line and substrate. Without proper passivation there is current leakage from the n^+ bit lines to the *p*-type substrate, leading to signal loss and power consumption. This leakage has been minimized by growing a sacrificial oxide to consume the damaged silicon and then regrowing a high-quality thermal oxide to complete passivation. The third critical processing area is planarization of the TEOS oxide. The silicon pillar tops must be exposed for electrical conductivity but must not be eroded to maintain sufficient diode reverse breakdown voltage for writing. Both the use of a hard silicon nitride layer to stop the CMP and a post-CMP highly selective wet-chemical etch are being explored for endpoint control.

Single bits at 0.25-μm diameter and memory arrays at 0.6 μm have been successfully fabricated and tested. Checkerboards and other patterns have been programmed in small arrays. Programming can be accomplished one word at a time with single 12-V, 1-μs pulses.

A new reticle set has been designed that includes arrays with selection circuitry and deep-ultraviolet lithography capability. The selection circuitry will allow on-chip decoding of a 4-kbit memory array. The bit selection is performed by *p*-channel MOS pass transistors. These transistors are fabricated in the *n* epitaxial layer, and transistor isolation is provided by the silicon etches required for the memory array. The reticle set includes arrays with feature sizes down to 0.3 μm using 248-nm lithography.

S. P. Doran   P. W. Wyatt
H. I. Liu   T. M. Lyszczarz

REFERENCES

1. *Solid State Research Report,* Lincoln Laboratory, MIT, 1994:2, p. 35.

2. *Solid State Research Report,* Lincoln Laboratory, MIT, 1992:4, p. 25.

REPORT DOCUMENTATION PAGE

Form Approved
OMB No. 0704-0188

1. AGENCY USE ONLY (*Leave blank*)	2. REPORT DATE 15 November 1995	3. REPORT TYPE AND DATES COVERED Quarterly Technical Report, 1 August–31 October 1995

4. TITLE AND SUBTITLE

Solid State Research

6. AUTHOR(S)

David C. Shaver

5. FUNDING NUMBERS

C — F19628-95-C-0002
PE — 63250F
PR — 221

7. PERFORMING ORGANIZATION NAME(S) AND ADDRESS(ES)

Lincoln Laboratory, MIT
244 Wood Street
Lexington, MA 02173-9108

8. PERFORMING ORGANIZATION REPORT NUMBER

1995:4

9. SPONSORING/MONITORING AGENCY NAME(S) AND ADDRESS(ES)

HQ Air Force Materiel Command
AFMC/STSC
Wright-Patterson AFB, OH 45433-5001

10. SPONSORING/MONITORING AGENCY REPORT NUMBER

ESC-TR-95-096

11. SUPPLEMENTARY NOTES

None

12a. DISTRIBUTION/AVAILABILITY STATEMENT

Approved for public release; distribution is unlimited.

12b. DISTRIBUTION CODE

13. ABSTRACT (*Maximum 200 words*)

This report covers in detail the research work of the Solid State Division at Lincoln Laboratory for the period 1 August–31 October 1995. The topics covered are Electrooptical Devices, Quantum Electronics, Materials Research, Submicrometer Technology, High Speed Electronics, Microelectronics, and Analog Device Technology. Funding is provided primarily by the Air Force, with additional support provided by the Army, ARPA, Navy, BMDO, NASA, and NIST.

14. SUBJECT TERMS

electrooptical devices	high-speed electronics	lasers	field-effect transistors
quantum electronics	microelectronics	thermoelectric materials	charge-coupled devices
materials research	analog device technology	silylation resists	microwave resonators
submicrometer technology	digital integrated circuits	diamond field emission	read-only memories

15. NUMBER OF PAGES 78

16. PRICE CODE

17. SECURITY CLASSIFICATION OF REPORT	18. SECURITY CLASSIFICATION OF THIS PAGE	19. SECURITY CLASSIFICATION OF ABSTRACT	20. LIMITATION OF ABSTRACT
Unclassified	Same as Report	Same as Report	Same as Report